TURKISH REPUBLIC
ANKARA UNIVERSITY
GRADUATE SCHOOL OF HEALTH SCIENCES

DEVELOPMENT OF A DISPOSABLE MIP-BASED ELECTROCHEMICAL SENSOR FOR DETERMINATION OF THE ANTIVIRAL DRUG

Mohammad MEHMANDOUST

DEPARTMENT OF ANALYTICAL CHEMISTRY

MASTER'S THESIS

SUPERVISOR

Prof. Dr. Nevin ERK

ANKARA

2022

TURKISH REPUBLIC
ANKARA UNIVERSITY
GRADUATE SCHOOL OF HEALTH SCIENCES

DEVELOPMENT OF A DISPOSABLE MIP-BASED ELECTROCHEMICAL SENSOR FOR DETERMINATION OF THE ANTIVIRAL DRUG

Mohammad MEHMANDOUST

DEPARTMENT OF ANALYTICAL CHEMISTRY

MASTER'S THESIS

SUPERVISOR

Prof. Dr. Nevin ERK

ANKARA

2022

Statement

Ankara University

Ankara University Institute of Health Sciences

I hereby declare truthfully that this thesis is my original work; that I followed scientific and ethical principles and rules throughout the stages of preparation, data collection, analysis, and presentation of my work; and that I cited the sources of all data and information obtained within the scope of this study and included these sources in the references section; and that this study has been scanned for plagiarism with Turnitin program used by Ankara University, and that it does not have any plagiarism whatsoever.

Name and surname of student: Mohammad Mehmandoust

Date: 04/07/2022

Signature:

LIST OF CONTENTS

LIST OF ABBREVIATIONS

2-AP	2-aminophenol
AFM	Atomic force microscopy
AIDS	Acquired immunodeficiency syndrome
AIBN	Azobisisobutyronitrile
B-R	Britton–Robinson buffer
CA	Chronoamperometry
CV	Cyclic voltammetry
$C_3H_{12}N_6O_3$	Guanidine carbonate
D	Diffusion coefficient
DPV	Differential pulse voltammetry
DVB	Divinylbenzene
EIS	Electrochemical impedance spectroscopy
EGDMA	Ethylene glycol dimethacrylate
FTIR	Fourier transform infrared spectroscopy
FDA	US Food and Drug Administration
HOMO	Highest occupied molecular orbital
H_2PtCl_6	Chloroplatinic acid
HCl	Hydrochloric acid
HNO_3	Nitric acid
H_2SO_4	Sulfuric acid
HPLC	High-performance liquid chromatography
HIV	Human immunodeficiency virüs
$K_3Fe(CN)_6$	Potassium hexacyanoferrate (III)
$K_4Fe(CN)_6$	Potassium hexacyanoferrate (II)
LUMO	Lowest unoccupied molecular orbital
LC-MS	Liquid chromatography-mass spectrometry
LOD	Limit of detection
MIPs	Molecularly imprinted polymers

MAA	Methacrylic acid
NIPs	non-imprinted polymers
NtRTI	Nucleotide analogue reverse-transcriptase inhibitor
NIPAm	N-isopropyl acrylamide
NaOH	Sodium hydroxide
$NaBH_4$	Sodium borohydride
NH_4SCN	Ammonium thiocyanate
Pt@g-C_3N_4/F-MWCNTs	Platinum nanoparticles/graphitic carbon nitride/functionalized multiwalled carbon nanotubes
PETRA	Pentaerythritol triacrylate
SEM	Scanning electron microscopy
SPE	Solid-phase extraction
SPCE	Screen-printed carbon electrode
TNF	Tenofovir
TFMAA	2-(trifluoromethyl)acrylic acid
TRIM	Trimethylolpropane trimethacrylate
UV-Vis	Ultraviolet-visible spectroscopy
XRD	X-ray diffraction
ΔEp	Peak-to-peak separation
α	Electron transfers coefficient

LIST OF FIGURES

LIST OF TABLES

1. INTRODUCTION

Antiviral medicines are medications that combat viral infections (Balfour Jr, 1999). Many viral infections have no effective antiviral medicines (Tompa ve ark., 2021). However, there are many influenza medications, a few herpes virus treatments, and several novel antiviral drugs to treat human immunodeficiency virus (HIV) and hepatitis C infections. Antiviral medicines are a type of antiviral treatment that is used to treat viral infections. A broad-spectrum antiviral is effective against many viruses, whereas most antivirals target specific viruses. Antiviral medications, unlike most antibiotics, do not kill their target pathogen; in place of, they obstruct it from growing. Antiviral medications are one type of antimicrobial, including antibiotics, antifungal, antiparasitic treatments, and monoclonal antibody-based antiviral therapies (Spirescu ve ark., 2021). Antivirals are generally believed to be safe for the host; therefore, they can be utilized to treat infections. They must be distinguished from viricides, which are not medications and instead deactivate or kill viral particles inside or outside the body. The majority of antiviral medications on the market today are intended to treat HIV, herpes viruses, hepatitis B and C viruses, and influenza A and B viruses. Herpes and other viral infections can be treated with nonretroviral antiviral medicines. Although the incidence of nephrotoxicity caused by these medicines has not been determined, they appear to be capable of causing renal failure via a variety of pathways. Nephrotoxicity can be caused by acyclovir, adefovir dipivoxil, cidofovir, tenofovir, and valacyclovir, at least partly due to a direct effect influence on renal tubular function. Proteinuria, azotemia, glycosuria, metabolic acidosis, and, in rare cases, Fanconi syndrome are all symptoms of cidofovir nephrotoxicity. Antiviral medication development tactics are divided into attacking viruses directly or targeting host cell components. Attachment inhibitors, entrance inhibitors, uncoating inhibitors, protease inhibitors, polymerase inhibitors, nucleoside and nucleotide reverse transcriptase inhibitors, nonnucleoside reverse transcriptase inhibitors, and integrase inhibitors are examples of direct virus-targeting antiviral medicines. Protease inhibitors (darunavir, atazanavir, and ritonavir) and viral DNA polymerase inhibitors (acyclovir, valacyclovir, valganciclovir, and tenofovir) are among the Top 200 Drugs by Sales in the 2010s. Since the introduction of HIV in 1981, the disease has become a major human problem in recent decades (Alonzo ve Reynolds, 1995). HIV is the name of the virus that results in acquired immunodeficiency syndrome (AIDS). The body`s immune system breaks down, causing deadly infections and some cancer. The virus can

be transmitted to another healthy person through certain secretions from a person infected with the virus (Lowenthal ve ark., 2014; Peacock-Villada ve ark., 2011). AIDS is an acquired immunodeficiency condition characterized by significant T cell depletion and more than 20 typical degenerative and neoplastic illnesses (Duesberg, 1989). Extensive research on people living with AIDS has shown that infection with the virus usually occurs long before the onset of symptoms; this interval, called the incubation period, is very variable in AIDS and lasts an average of 10 years (Siberry ve ark., 2012), and symptoms appear when the virus destroys the immune system (Wassner ve ark., 2020). Tenofovir (TNF) suppresses HIV reverse transcriptase activity by competing with deoxyadenosine 5′-triphosphate and the following incorporation into DNA via DNA chain termination (Kumar ve ark., 2013). Besides, tenofovir, as a nucleotide (nucleoside monophosphate) analogue, has potent activity against retroviruses and hepadnaviruses. Moreover, TNF is the first nucleotide analogue reverse-transcriptase inhibitor (NtRTI) to have been licensed to treat HIV infection by the US Food and Drug Administration (FDA) (Fernandez-Fernandez ve ark., 2011).

The widespread use of TNF for medicinal purposes with maximum therapeutic effects and minimum toxicities necessitates developing an accurate, sensitive, and rapid method for detecting TNF in real samples. Therefore, an accurate and cost-effective quantitative assessment of TNF in biological fluids from a validated analytical process is necessary to avoid its deleterious side effects and control its concentration. In the last decade, electroanalytical techniques have been widely used to assay drugs in pharmaceutical dosage forms and biological samples. Up to date, the quantification of TNF in pharmaceutical dosage form and the biological specimen has been presented using various techniques, including high-performance liquid chromatography (HPLC), UV-VIS, and liquid chromatography-mass spectrometry (LC-MS). For example, Kandagal et al. developed a straightforward reverse-phase high-performance liquid chromatographic method for TNF determination in pharmaceutical formulations and human plasma samples (Kandagal ve ark., 2008). The standard curve showed a wide linear concentration range of 0.2–10 μg/ml (R^2=0.9966). Moreover, Nevase et al. proposed a simple, quick, and accurate spectrophotometric method for TNF quantitative estimation in bulk and tablet (Nevase ve ark., 2011). Dissolved TNF in methanol demonstrates absorption at about 260.0 nm, and the method obeys Beer's law at the concentration range of 10-100 μg/mL. Finally, this approach showed a satisfactory recovery.

Despite the reliability and selectivity of the aforementioned methods, these approaches are usually intricate, necessitating expensive instruments and manual operations, such as adjusting chromatographic settings and pre-treatment of HPLC samples. Recently, researchers have paid more attention to electrochemical approaches to address the obstacles of the traditional methods due to their ease of use, sensitivity, simple operation, lower reagent consumption, versatility, rapid response miniaturization, and the possibility of improving their selectivity and specificity using developing electrode surface by conductive nanocomposite (Deroco ve ark., 2018). However, because many interferents are present during real sample analysis, selectivity is an inherent limitation in sensor performance, and restricting their use while extending the electrode surface can address this problem.

1.1. Analysis methods available for the active ingredient Tenofovir to date

Accordingly, Festinger et al. designed an electrochemical sensor based on a silver amalgam electrode and graphene oxide on a glassy carbon electrode to determine TNF in real samples (Festinger ve ark., 2022). However, this study suffers from significant sensitivity, and this type of electrode has its origin in the undesirable crystalline structure of silver (Baś ve Kowalski, 2002). In general, the main issue with existing studies is that they assume a costly approach and trade-off between sensitivity and dynamic range. Unfortunately, these conditions cannot be met in a point-of-care or a resource-limited climate; for example, the aptamer-based biosensor for TNF determination enhances the system's noise (Aliakbarinodehi ve ark., 2017), and the DNA in the created TNF biosensor is readily destroyed, necessitating precise storage and analysis settings, such as specific media or a buffer to keep the DNA stable and attached to the transducer. (Morawska ve ark., 2018). Moreover, the low-cost and nontoxic electrode is suitable for TNF determination but does not show appropriate stability (Chihava ve ark., 2020). For instance, Ozcelikay et al. developed a reliable and rapid voltammetric technique for TNF determination from its dosage form, based on its electrochemical oxidation on a glassy carbon electrode surface using two SWV and DPV (Ozcelikay ve ark., 2017). This developed method showed a wide concentration range from 0.6 up to 60.0 μM with a low limit of detection of 0.1 and 0.0084 μM for DPV and SWV, respectively. In contrast, sensor modalities using molecularly imprinted polymers (MIPs) instead of traditional methods can offer a higher level

of simplicity and accuracy. Therefore, a study is required to understand the limitation of TNF electrodes in a low-cost environment and to identify the best strategy, e.g., whether to use a MIP method with a high electroactivity.

1.2. Develop the electrode

MIPs are macromolecular polymeric species with unique and selective recognition sites in the polymer matrix for the template analyte molecule (Yoshikawa ve ark., 2016). MIPs are among the most widely used materials as recognition elements or modifiers in constructing modified electrodes to determine various analytes in recent years. MIPs are formed by polymerizing functional monomers in the presence of a template molecule, which is often the target analyte or a molecule of comparable size and chemical activity. When the template is removed, 3D molecular recognition cavities are produced that are complementary in size, shape, and chemical functionality, and these sites may re-adsorb the target molecules with specificity to offer enough selectivity in the analysis (Shaabani ve ark., 2021).

Generally, the MIPs are prepared using a variety of ways depending on their desirabilities, such as controlled free-radical polymerization, photopolymerization, evanescent-wave polymerization, and electro-polymerization. However, the electro-polymerization approach is preferable for preparing MIPs owing to its superior reproducibility, ease of polymer thickness control, high adhesion to the sensor surface, ease and fast execution, quick and straightforward, as well as the thickness and morphology of the MIP films can be controlled by different polymerization conditions (Blanco-Lopez ve ark., 2004; X. Sun ve ark., 2019). Therefore, to upgrade the sensitivity and selectivity of the electrochemical sensors, recognition elements are required that MIPs are good candidates, providing electrochemical sensors with specific recognition properties. Importantly, designing based on MIPs can reach the optimum condition only for their designed configuration. However, it is challenging to identify design strategies to further improve the MIP performance without a more fundamental understanding of the nanocomposite.

Depending on the polymerization media, 2-aminophenol (2-AP) polymerization can proceed through the oxidation of hydroxyl or amine groups, leading to various structures and these chemical groups enable the polymer to form strong hydrogen bonds with different analytes (Kadivar ve Aliakbar, 2019). These capabilities exhibit that poly 2-AP is a superior alternative for synthesizing a MIP to increase the sensitivity and selectivity of the developed electrode (Menon ve ark., 2018). Therefore, choosing and synthesizing the appropriate material is necessary to construct an efficient MIP-sensor for specific applications.

In recent decades, thanks to tremendous advances in nanotechnology, carbon-based materials such as carbon black, graphite, single-walled carbon nanotubes, and multi-walled carbon nanotubes are becoming an essential modifier for the determination features of spices in biological systems. On the other hand, to improve the detection ability of the analytes, the nanomaterials are modified onto the electrode surface.

In recent years, multi-walled carbon nanotubes (MWCNTs) have been widely used to detect electroactive materials because of their excellent adhesion, high electrical conductivity, and porous structure (Gopi ve ark., 2021). Because of these characteristics, MWCNTs can be utilized as electrode support materials to improve the electron transfer rate and electrochemical performance to detect analytes. However, more study is required to overcome the limitations faced by MWCNTs based on electrocatalysts to decrease overpotential and boost current densities and stability. To address this issue, graphitic carbon nitride (g-C_3N_4) can be embedded on the surface of the MWCNT. Recently, g-C_3N_4 has attracted considerable interest in both electrochemical sensing and electrocatalysis because of its exceptional strength, electrical conductivity, and chemical stability. Moreover, platinum nanoparticles (Pt NPs) conjugation with F-MWCNT and g-C_3N_4 remarkably enhances the electrocatalytic performance of the developed electrode, with faster electron transfer and effective carrier collection. As a result, it is reasonable to speculate that integrating the multi-walled carbon nanotubes with graphene carbon nitride and platinum nanoparticles also exerts the same function in electrochemical sensors and electrocatalysis. Therefore, we attempted to construct a MIP-sensor using MWCNT, g-C_3N_4, and Pt NPs in this work. There is no published study about an effective method to detect TNF based on the molecularly imprinted polymer with innovative nanocomposite.

Inspired by these ideas, in this work, we have designed and fabricated a nanocomposite based on molecularly imprinted polymers and experimentally demonstrated its sensing performance by studying the TNF interaction with specific sites on the electrode surface for the first time. The developed nanocomposite on the screen-printed electrode (Pt@g-C_3N_4/F-MWCNT/SPCE) toward the voltammetric determination of antiviral agents TNF was investigated using the DPV method, which showed a linear concentration range of 0.005 to 0.69 μM with LOD of 0.003 μM. The advanced voltammetric technique based on nanocomposite shows good sensitivity and selectivity for TNF determination in actual samples such as human plasma, water, and urine samples. It can now be envisaged that the results demonstrated that the imprinted sensor represents a potentially inexpensive, fast, accurate, and reliable alternative approach for the ultrasensitive detection of antiviral drugs.

1.3. Molecular Imprinting

The contact process between diverse biomolecules such as proteins, nucleic acid, carbohydrates, and lipids in biological systems is known as molecular recognition. Inspired by natural molecular recognition processes, molecular imprinting creates polymeric molecular recognition units that are more resilient, cost-effective, and have similar affinity and selectivity for the template as their biological counterparts. By polymerizing functional monomers and crosslinkers around a template species, molecular imprinting may be employed to construct synthetic receptors. After removing the template from the polymer matrix, voids remain chemically and sterically selective for the imprinted molecule. MIPs, or molecularly imprinted polymers, are the name given to these polymers. Covalent and non-covalent interactions between monomers and templates during synthesis are the two types of interactions during molecular imprinting. The preorganization of functional monomer around a target analyte, also known as the template, is the initial stage in MIP synthesis (Fig. 1.1). Second, the monomers are arranged in a complex around the template, then polymerized using a crosslinker to keep the complex in place; lastly, the analyte is removed after polymerization by washing the resulting MIP containing specific binding sites for the template molecule.

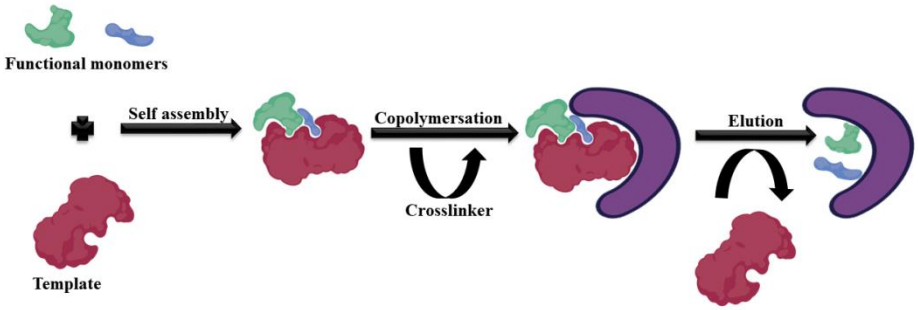

Figure 1.1. Illustration of the preparation of molecularly imprinted polymers.

1.4. Several imprinting approaches

MIPs are developed to selectively detect and bind a certain component in a complicated combination of compounds. The recognition is based on complementary interactions between the target molecule's functional groups and the polymer cavities. Three sorts of preparation approaches were developed as a result of different interactions. Despite their conceptual differences, both approaches follow the same three-step process. The recognition monomer(s) form a ring around the target molecule at first. In the presence of a porogen solvent, the former is copolymerized with a crosslinking agent. The copolymer's high crosslinker content ensures structural stiffness, allowing pores to form within the polymer matrix that is comparable in size, shape, and morphology to the target molecule following template extraction.

1.4.1. Covalent Imprinting

The template is transformed into a polymerizable molecule and copolymerized in covalent imprinting. As a result of the covalent bonding between monomers and targets, the template may maintain its exact orientation throughout the polymerization process. Cleaving the polymer-template bond is needed to remove the target from the matrix. The covalent bonds

are repaired during rebinding. Because acids may react quickly and reversibly with diols, they've been commonly utilized in this sort of preparation (Leite ve ark., 2014).

1.4.2. Semi-covalent Imprinting

Covalent contacts are used during polymerization in a semi-covalent method, whereas non-covalent interactions are used for rebinding (Puzio ve ark., 2013). Fig. 1.2 indicates a representation of the technique utilized by C.Cacho et al. (Cacho ve ark., 2006). The scientists employed an amide bond in their study, using propazine methacrylate as the template, ethylene glycol dimethacrylate as the cross-linker, and toluene as the porogen. The analyte was then hydrogen-bonded back into the cavities in a nonpolar organic solvent (methanol).

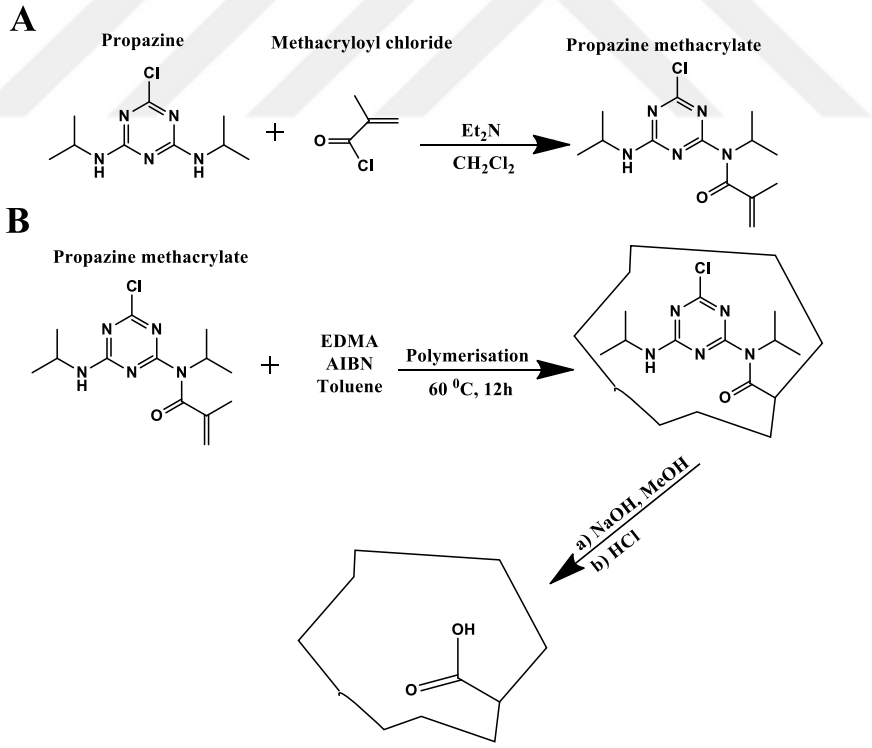

Figure 1.2. The propazine methacrylate synthesis (A) and subsequent polymer preparation (B) are the reaction scheme.

1.4.3. Non-covalent Imprinting

The most often utilized preparation approach is non-covalent imprinting (Hwang ve Lee, 2002; H. Zhang ve ark., 2006). Imprinting and rebinding in this situation rely on non-covalent interactions between monomer and template. In several circumstances, hydrogen bonding is used (Del Sole ve ark., 2009; Hashim ve ark., 2014); Subhra Mohapatra et al. created MIP-nanoparticles through methacrylic acid (MAA), ethyl alcohol, and N-isopropyl acrylamide (NIPAm) as hydrogen-bonding, negatively charged, and hydrophobic functional monomers for atrial natriuretic peptides (C. Wang ve ark., 2011).

1.5. Comparing the imprinting approaches

Because the monomer-template arrangement is properly aligned and more permanent, covalent imprinting is often regarded as the approach that produces the best binding sites (uniform, well-defined, high binding affinity) (Andersson, 2000). However, there is a serious lack of flexibility with this approach. It necessitates the creation of a template derivative that can be polymerized for each polymer system. In addition, in mild circumstances, the link that holds the template in place during polymerization should be easily produced and severed. Non-covalent imprinting, on the other hand, produces some non-specific sites but may use a wide range of commercially available monomers. Furthermore, target removal is as simple as extraction, and rebinding is as simple as mixing (Martín-Esteban, 2013; Tamayo ve ark., 2007).

1.6. Preparation techniques

Until recently, bulk polymerization was the most popular method for making MIPs (Mohajeri ve ark., 2011; Turiel ve Martin-Esteban, 2004). Despite its widespread use in the realm of imprinting technology, the word bulk is deceptive (Branger ve ark., 2013). Bulk

polymerization, in general, is defined as the polymerization of monomer alone, with no solvent present throughout the process (Gimenez ve ark., 2000). The preparation of complicated polymers that must be ground to yield a large imprinted surface area is described in studies detailing the synthesis of bulk molecularly imprinted polymers (Ansari ve Karimi, 2017; Speltini ve ark., 2017). Free radical polymerization of monomers in the same solvent volume is commonly used to create these polymers. At first, the liquid seems to be homogenous, but gaps in the polymer network form when polymer chains build and precipitate out. Grinding produces unevenly shaped particles with a high polydispersity of sizes. They usually need to be sieved, resulting in the loss of over 80% of the original polymer: just 20% of the particles are of usable size. Numerous laboratories have been working on creating polymerization processes that create consistently shaped and monodispersed particles in recent years. Therefore, polymerization can be divided into several categories, including emulsion polymerization, miniemulsion polymerization, suspension polymerization, precipitation polymerization, and imprinting inorganic particles.

1.7. Components of MIPs

The components of MIP particles, including template, functional monomers, cross-linking species, polymerization solvent, and initiator species, all play a role in successfully synthesizing MIP particles (Song ve ark., 2021). As a result, these components can affect the characteristics of the resulting MIPs, such as shape, morphology, selectivity, and solubility.

1.7.1. Functional Monomers

The binding points inside an imprinted polymer's binding sites created by self-assembly around a template molecule are formed by functional monomers (Renkecz ve ark., 2013). The structure of the recognition site is determined by the functional monomers utilized, while the concentration affects the number of binding sites in MIPs. The usage of functional monomers

is required to maintain stable monomer-template complexes during the imprinting process, and the best functional groups are selected to compliment the template molecule's chemical activity. For instance, in molecules with acidic groups, monomers with basic functionality are preferable compared to acid functionality and vice versa. For example, MAA is often utilized for basic templates. However, 2-(trifluoromethyl)acrylic acid (TFMAA) has been recently employed as a functional monomer for basic templates to boost selectivity and affinity over MAA. The chemical structure of the most common monomer is shown in Fig. 1.3. Therefore, functional monomer selection is critical for creating specific holes for the template molecule.

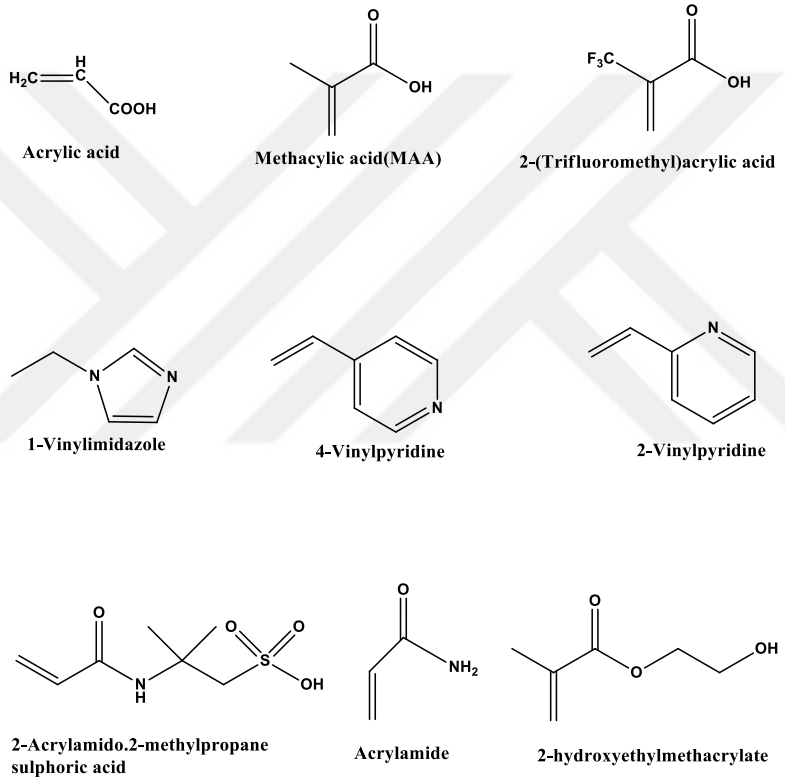

Figure 1.3. Structure of the most common monomers used for molecular imprinting.

In the polymerization process, monomers' electron and proton transfer play an essential role in forming polymer films. A polymerization process for 2-AP has been proposed by Mohammad Kadivar and colleagues (Figure 1.4).

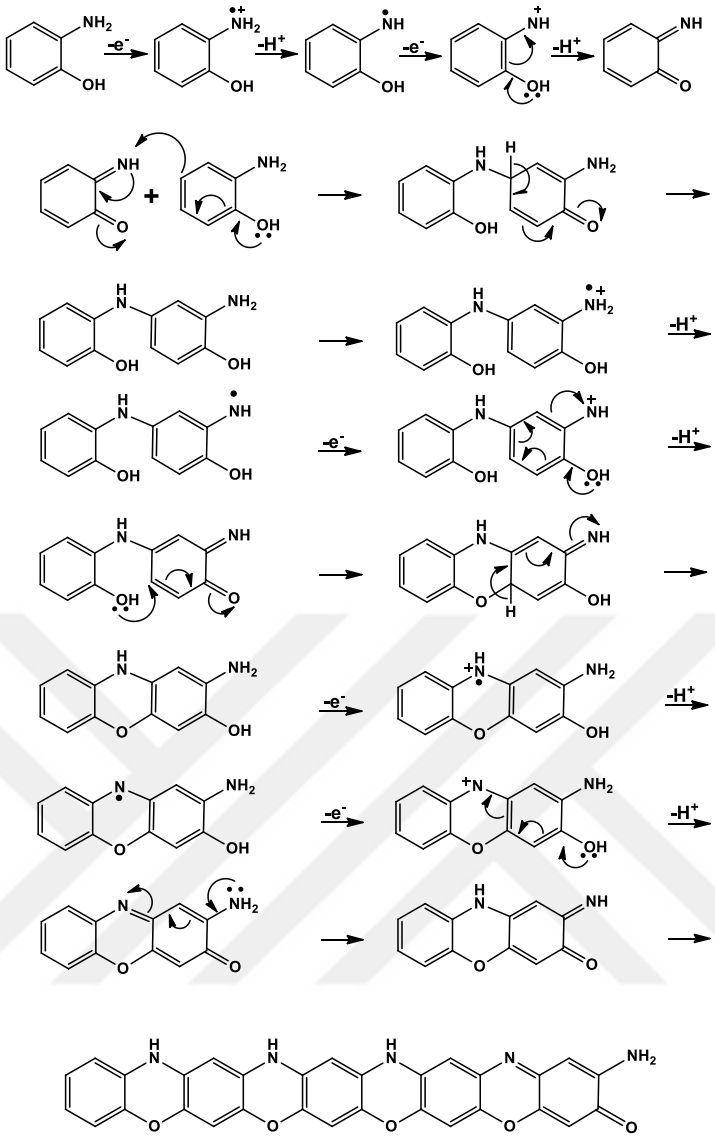

Figure 1.4. The proposed polymerization mechanism of 2-AP (Kadivar ve Aliakbar, 2021).

1.7.2. Template

The template also plays a crucial function in the molecular imprinting process to construct an active polymer film. Owing to the chemical bonds that may be established between the monomer and template, the chemical structure of a template dictates the type of monomer that could be utilized in the polymerization procedure, dictating the amount of molecular recognition and the effectiveness of molecular imprinting. The kind of interaction sites, number

of contacts, template shape, and monomer-template complex stiffness influence the polymer's binding strength and selective recognition. Polymers with high specificity and affinity are formed using templates with numerous binding locations for functional monomers.

In certain situations, the template molecule's shape and size are adequate to provide a complementary binding site unique to a molecule's steric isomer. Templates with higher structural stiffness have a higher affinity and selectivity for the polymer cavity. On the other hand, protein imprinting can be complex since proteins can change their shape and the positions of any charged atoms. When selecting a template molecule, several considerations must be taken into account. These factors include the molecule's solubility in the chosen solvent and its electrostatic functions.

1.7.3. Cross-linking Monomers

Cross-linking monomers employ two or more double bonds to create functional groups to construct a cross-linked network of polymer chains. The most common cross-linkers are shown in Fig. 1.5 and are commonly employed in scientific research. The cross-linker has three basic functions:

1- It is necessary to influence the shape of the polymer matrix.

2- It contributes to the imprinted binding site's stability.

3- It gives the polymer matrix mechanical stability.

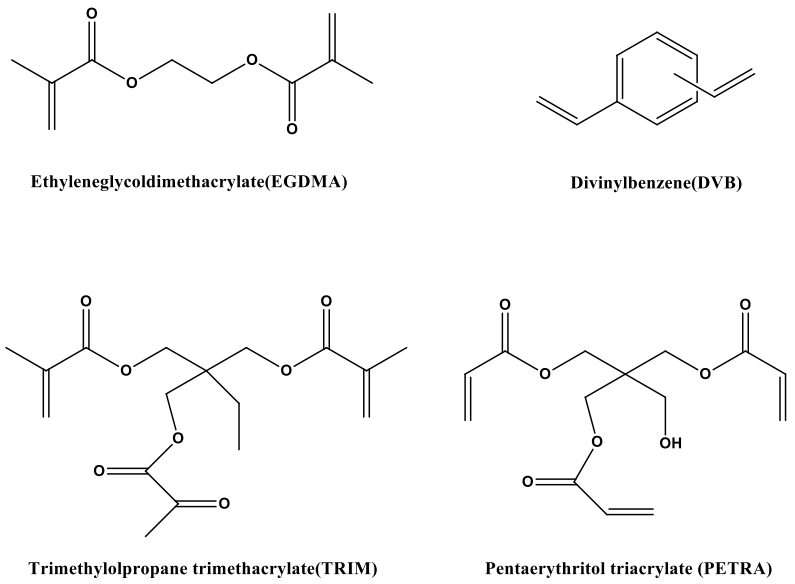

Figure 1.5. Structure of common cross-linkers.

Recently, significant volumes of cross-linking monomers have been used to develop permanently porous materials with suitable mechanical stability during polymerization. On the other hand, the main task of a cross-linker is to stabilize the polymer's binding sites by generating a strongly cross-linked stiff polymer network. Furthermore, large volumes of crosslinking monomers are frequently necessary to assure the polymer's accessibility and mechanical strength.

Maintaining the binding specificity of an imprinted polymer requires the right amount of cross-linking so that a low amount of cross-linker (less than 20%) might reduce the selectivity of MIPs. Conversely, if the amount of cross-linkers increases (over 80%), the polymers' loading capacity might be diminished, hampering the substrate diffusion into the imprinted sites. In recent publications, ethylene glycol dimethacrylate (EGDMA) was used as the crosslinking monomer. The loading capacity of this composition is excellent, and the template resolution might be increased. However, trimethylolpropane trimethacrylate (TRIM) was added to the polymerization mixture, resulting in polymers with better recognition characteristics than EGDMA due to TRIM containing one more vinyl group compared to EGDMA; therefore, it requires less monomer to produce the same backbone stiffness, contributing to binding specificity.

1.7.4. Solvent

The solvent is a crucial component of the polymerization mix because it aids in the creation of monomer-template complexes (Vasapollo ve ark., 2011). Electrostatic interactions are hence more important in hydrophobic liquids. When employed in non-covalent-based imprinting, polar solvents tend to cause prepolymer complex dissociation, especially for protic solvents. The most often utilized solvents for MIP synthesis include toluene, chloroform, dichloromethane, and acetonitrile. The solvent also controls the geometry and size of pores generated in macroporous polymers by bringing all of the MIP components into one phase in the polymerization mixture.

Furthermore, the kind and amount of the porogenic solvent utilized in the polymerization affect the imprinting process. The porogen must be carefully studied in non-covalent imprinting to ensure that the solvent favors the development of the template-monomer complex while not interfering with the interactions between the functional monomers and template molecules.

1.7.5. Initiator

The most common method for making MIPs is free radical polymerization. In general, synthesis is carried out in bulk or solution under mild reaction conditions with temperatures below 80°C and at atmospheric pressure. It may be used to represent a variety of functional groups and template molecules. As the first radical source, various chemical initiators with various characteristics can be utilized. In most cases, initiators are utilized at a low concentration compared to the monomers and cross-linkers (about 1%). The most common initiators to produce MIPs are shown in Fig. 1.6. To start and regulate the rate and method of initiator breakdown, heat or light exposure can be utilized. For instance, The azo-based initiator azobisisobutyronitrile (AIBN) may be decomposed by UV radiation or thrombolysis to produce stabilized carbon-centered radicals capable of forming vinyl polymers.

A quick termination process ensues when the UV light is turned off in an inverter-controlled polymerization reaction. Overall, inverter-controlled photo-started polymerization results in MIPs with better recognition characteristics than thermally initiated polymerization. However, because of the presence of oxygen in the air and dissolves in the solution, it must be removed from the polymerization mixture to avoid interfering with free-radical polymerizations. Purging the monomer solution with nitrogen gas does this.

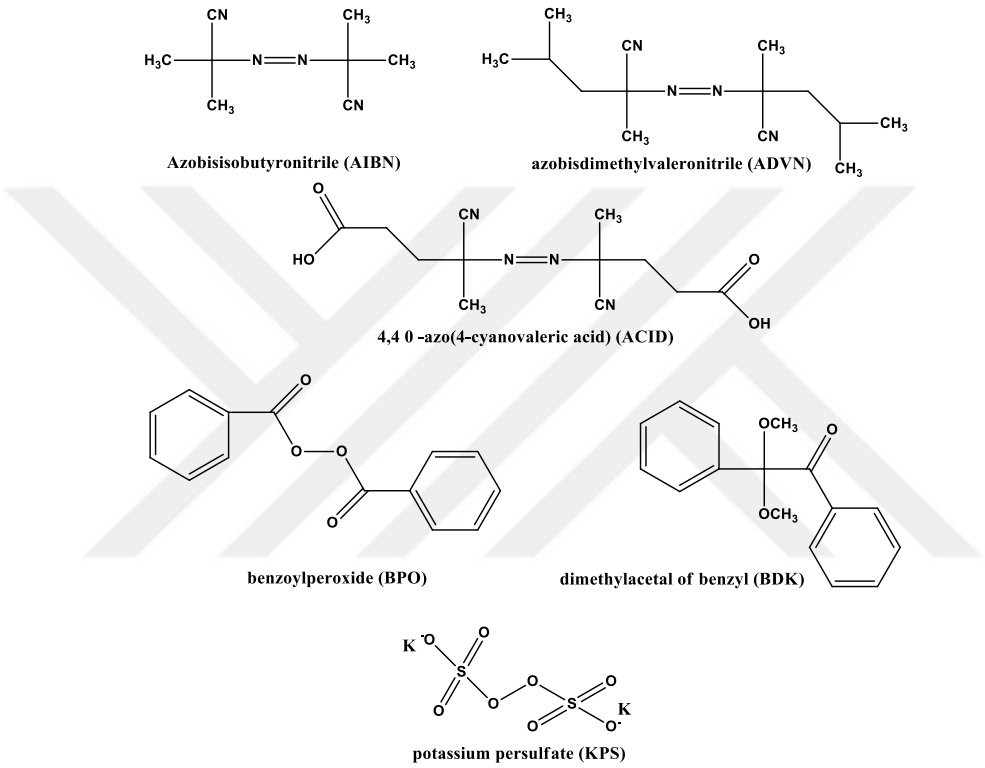

Figure 1.6. Chemical structures of typical initiators used in molecular imprinting.

2. GENERAL INFORMATION

2.1. Detection Methods

Various electrochemical approaches can be utilized to detect analytes, each having benefits and drawbacks that vary depending on the design of the electrochemical cell and the selective component inside the device. The next part explains the basics of electrochemical methods and shows how they've been used to identify medicinal compounds.

2.1.1. Potentiometry

Potentiometry is a well-known method for measuring the differences in potential between a working electrode (which is usually ion-selective) and a reference electrode; Figure 2.1 shows a schematic of the corresponding electrochemical cell. Because of their speedy, low-cost, and accurate analysis, these devices have been widely employed in various domains, such as analytes diagnostics, industrial process control, and environmental monitoring.

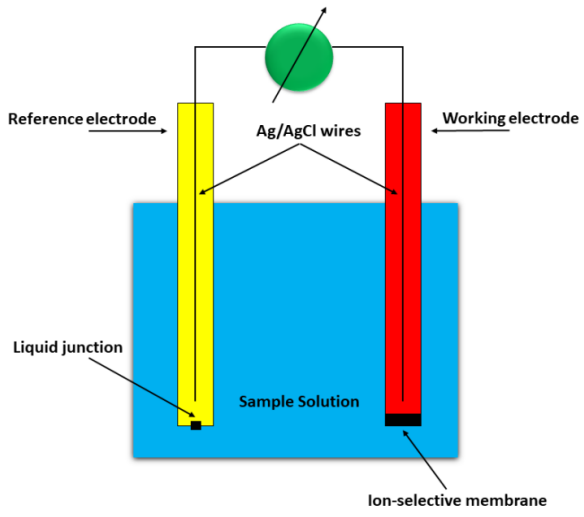

Figure 2.1. Representation of the potentiometric electrochemical cell.

The pH electrode, primarily built on a glass membrane, is the most typical example of this classic technique. It is owing to the electrode's extraordinarily strong hydrogen ion selectivity, wide response range, and quick and steady response. But, recent advancements in sensor manufacturing wafer technology have increased the number of reported chip-based potentiometric devices that are low-cost and repeatable in batch production. Potentiometric devices may be included in solid-state electronics and are excellent for sensor arrays due to their tiny size.

2.1.2. Voltammetry

2.1.2.1 Cyclic Voltammetry

The most extensively used approach for obtaining qualitative electrochemical reactions is cyclic voltammetry. In many electroanalytical studies, the first experiment is cyclic voltammetry. It allows for a quick determination of the electroactive species' redox potentials and a quick assessment of the influence of media on the redox process. The potential of a stationary working electrode (in an undisturbed solution) is linearly scanned using a triangle potential waveform in cyclic voltammetry (Figure 2.2). Single or several cycles might be employed depending on the information desired. A cyclic voltammogram is the current–potential graphic that results. Figure 2.3 depicts a reversible redox couple's predicted reaction throughout a single potential cycle. Only the oxidized form of O is thought to be present at first. As a result, a negative-going potential scan is picked during the first half-cycle, starting at a value where no reduction happens. A cathodic current grows as the applied voltage approaches the redox process's characteristic E° until a peak is attained. The direction of the potential sweep is reversed after reaching the potential area where the reduction process occurs (at least 90/n mV beyond the peak). During the reverse scan, R molecules collected near the surface during the forward half-cycle are reoxidized back to O, resulting in an anodic peak.

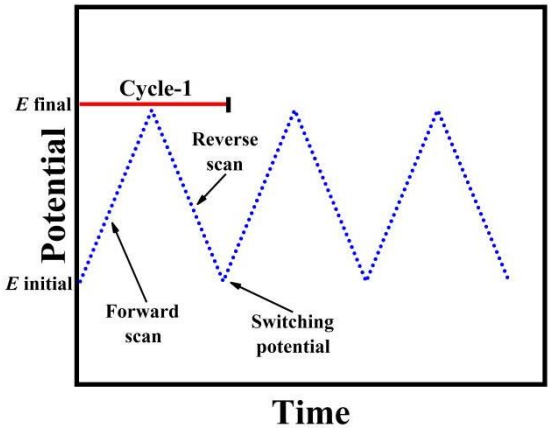

Figure 2.2. Potential-time excitation signal in a cyclic voltammetric experiment.

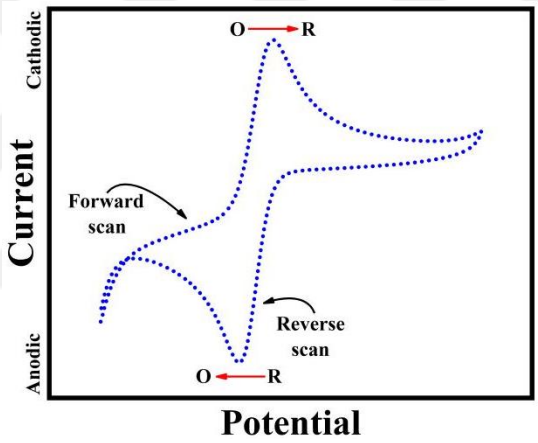

Figure 2.3. Typical cyclic voltammogram for a reversible $O+ne^{-}\leftrightarrow R$ redox process.

2.1.2.2. Differential Pulse Voltammetry

Differential-pulse voltammetry is a helpful approach for assessing trace amounts of various analytes. Fixed magnitude pulses overlaid on a linear potential ramp are supplied to the working electrode right before the end of the drop in differential-pulse voltammetry (Fig. 2.4).

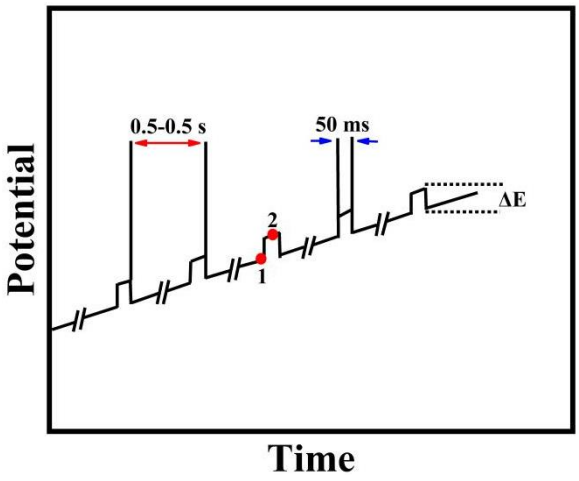

Figure 2.4. Excitation signal for differential-pulse voltammetry.

2.1.2.3. Impedance Spectroscopy

Impedance spectroscopy is a useful tool for examining the characteristics of chemically developed electrodes and determining electrochemical reaction rates. When a current runs through a circuit containing resistors, capacitors, and inductors, it encounters impedance, which is a complicated resistance (Fig. 2.5). Electronic equivalent circuitry components that match the observed impedance spectra can be used to describe electrochemical processes at the electrode–solution interface. The Randles and Ershler electrical equivalent-circuit model are useful for modeling interfacial phenomena.

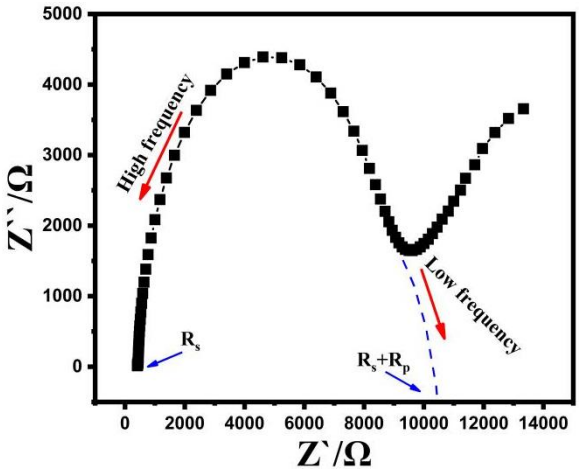

Figure 2.5. Faradaic impedance spectra showed in the form of a Nyquist plot.

2.1.2.4. Chronoamperometry

In chronoamperometry, the working electrode voltage is stepped from a value where no faradaic reaction betides to a value where the surface concentration of the electroactive species is nearly zero (Fig. 2.6 A). The solution is unstirred (quiescent), and the working electrode is stationary. The current–time dependency that results is observed. The current–time curve shows the change in the concentration gradient in the surface region since the mass transfer is purely through diffusion under these conditions. It includes the steady expansion of the diffusion layer as the reactant is depleted, resulting in a reduction in the slope of the concentration profile as time passes (see Fig. 2.6 B). According to these observations, the Cottrell equation (Eq 2.1) gives the current decays with time (Fig. 2.6 C).

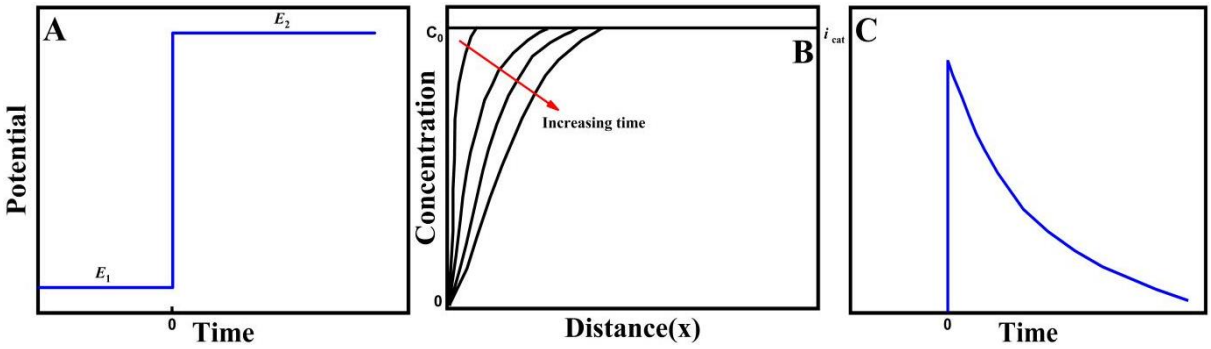

Figure 2.6. Chronoamperometric conditions: (a) potential–time waveform; (b) change in concentration profiles as time progresses; (c) the current–time response.

$$i(t) = \frac{nFACD^{\frac{1}{2}}}{\pi^{\frac{1}{2}} t^{\frac{1}{2}}} = kt^{\frac{-1}{2}} \quad \text{(Eq. 2.1)}$$

Here I indicates the current, n the number of transferred electrons, F the Faraday constant, A the active surface area of the electrode, C shows the bulk concentration, D the diffusion coefficient, and t the time.

2.2. The Aim of The Thesis

This dissertation addresses the investigation of TNF-specific molecularly imprinted polymers. The inspiration for this area of research stems from the promise that molecularly imprinted polymers have as artificial recognition components, mainly when used as the selective recognition element of a biosensor method. As previously stated, reports of imprinting methods in the aqueous phase are few (compared to classical imprinting approaches). As a result, the creation of MIPs for biological molecules of therapeutic value has received little attention.

2.3. Choice Materials

Pt@g-C_3N_4/F-MWCNT was utilized to construct a developed electrode to apply the synergetic effects to boost electrochemical activity, considering all of the aforementioned facts and the benefits of the MWCNT-based nanocomposite. Modified electrodes based on MWCNT have a comprehensive advantage for detecting target analytes: large active surface area, rich π-conjugation structure, superior in-plane conductivity, and a unique chemical and physical structure MWCNT. Moreover, the charge transfer might be enhanced through crystal texturing of Pt nanoparticles and g-C_3N_4. In particular, Pt NPs have high conductivity and huge specific surface areas. Therefore, Pt NPs are preferred because they increase selectivity at electrochemical sensors. Therefore, Pt@g-C_3N_4/F-MWCNT is selected as sensitive material to decorate electrodes.

3. EXPERIMENTAL and METHODS

Any electrochemical investigation's performance is heavily reliant on the working electrode. The electrode material will affect the signal-to-noise ratio, repeatability, redox behavior, charge transfer kinetics, and potential window. Furthermore, the electrode shape can significantly impact component diffusion to the electrode surface.

3.1. Devices

3.1.1. Potentiostat/Galvanostat Device

The electrochemical methods such as differential pulse voltammetry (DPV), cyclic voltammetry (CV), chronoamperometry (CA), and electrochemical impedance spectroscopy (EIS) were conducted using a MetrohmAutolab potentiostat/galvanostat system (PGSTAT128N, Metrohm, Herisau, Sweden, NOVA 2.1.1 version software). The experiments were performed by an electrochemical cell containing a screen-printed electrode.

3.1.2. Characterization Devices

The AFM analysis of the nanocomposite was VEECO Multimode 8 Atomic Force Microscope and Micromeritics Gemini VII surface area. SEM and EDX images were recorded in micrographs of the materials by ZEISS GeminiSEM 560 at 3.00 kV. Fourier transform infrared spectroscopy (FT-IR) spectra were observed on a PerkinElmer Spectrum. The X-ray diffraction pattern was observed using a Rigaku smart laboratory diffractometer (operated at 40 kV and 20 mA) with a Cu Kα source at a wavelength of 1.540 Å. BET analysis was also performed using gas auto-sorption (Gemini VII 2390 V1.03 (V1.03 t) (Micromeritics

Instrument Corp.). UV–Vis was observed using a double beam spectrophotometer (Shimadzu-Japan) model UV-1800.

3.1.3. Peripheral Devices

The ultrasonic bath (ISOLAB model) was used for mixing and solubilization processes. Deionized water (SartoriusArium ComfortI-1-UV-T model) was used to prepare the solutions. Magnetic Stirrer with Heater (Velp Scientifica model) was utilized for mixing solutions. An analytical electronic sensitive balance (OHAUS model) was used for the weighing process. The pH of the buffers was observed with a sensitive pH meter (Hanna Instruments, Woonsocket, Rhode Island, USA), and the pH solution was adjusted using 0.1 M NaOH and HCl.

3.2. Chemicals

Chloroplatinic acid (H_2PtCl_6, ≥37.50%), MWCNT (>98% carbon basis), nitric acid (HNO_3), sulfuric acid (H_2SO_4), hydrochloric acid (HCl), sodium hydroxide (NaOH), and sodium borohydride ($NaBH_4$) were purchased from Merck (Darmstadt, Germany). Ammonium thiocyanate (NH_4SCN), guanidine carbonate ($C_3H_{12}N_6O_3$), 2-Aminophenol (2-AP), potassium hexacyanoferrate (III) ($K_3Fe(CN)_6$), potassium hexacyanoferrate (II) ($K_4Fe(CN)_6$), L-ascorbic acid, L-cysteine, L-arginine, dopamine hydrochloride, glucose, and uric acid were acquired from Sigma-Aldrich Company (Germany). Human blood plasma specimens were also obtained from Sera-Flex Inc. Also, a urine specimen was obtained from a volunteer for use in the experiments. Tenofovir was purchased from Bristol Myers Squibb Inc.

3.3. Solutions Used

3.3.1. Preparation of Supporting Electrolytes

3.3.1.1. Preparation of Acetate Buffer

Firstly, 136.0 gr of sodium acetate and 77.0 gr of ammonium acetate were dissolved in water and diluted to 1000.0 mL with the same solvent. Then, 250.0 mL of glacial acid was added and mixed.

3.3.1.2. Preparation of Phosphate Buffer Saline

68.0 gr of potassium dihydrogen phosphate was dissolved in water and diluted with the same solvent. The buffer pH was adjusted using phosphoric acid.

3.3.1.3. Preparation of Citrate Buffer

4.8 gr of citric acid was dissolved in 80.0 mL of water. Buffer pH was adjusted using 1.0 M sodium hydroxide and hydrochloride.

3.3.1.4. Preparation of Britton–Robinson (B-R) Buffer

The supporting electrolytes for Britton-Robinson buffer were boric acid, phosphoric acid, potassium chloride, and acetic acid solutions, and their pH values were adjusted with 2.0 M NaOH and HCl.

3.3.2. TNF Stock Solution

A certain concentration of 1.0 mM TNF in deionized water was prepared. The stock solution with 0.1 M B-R buffer was diluted to prepare the requested concentration.

3.3.3. Human plasma Sample Preparation

The human blood serum and 1.0 mL of acetonitrile as a precipitating agent was centrifuged at 8000 rpm for 10 min and filtered. After filtration, it was diluted 10 times using a 0.1 M B-R buffer solution without further treatment.

3.3.4. Urine Sample Preparation

The urine sample was contributed by a volunteer. Before the real sample analysis, urine samples were centrifuged, and the supernatant liquid was used and carefully filtered using PTFE syringe filter (0.45 μm) membrane filters.

3.4. Synthesis

3.4.1. Synthesis of Functionalized MWCNT

2.0 g of MWCNT was functionalized using H_2SO_4 and HNO_3 (3:1 ratio), treated at 160 °C for 1 h vigorously. After cooling, the obtained product was filtered and washed three times with water and ethanol until the filtrate was found with neutral pH. The obtained materials were dried in a vacuum oven at 60 °C until constant weight (J. Sun ve ark., 2020). The purified MWCNT was collected for further use.

3.4.2. Synthesis of 2D-g-C_3N_4

The copolymerization technique was used for synthesizing g-C_3N_4. Ammonium thiocyanate and guanidine carbonate were firstly annealed separately at 500 °C. Afterward, the same amount of NH_4SCN and $C_3H_{12}N_6O_3$ were mixed and then heated at 600 °C for 6 h. The material obtained was cooled down to room temperature, and products were gathered after grinding (Sahoo ve ark., 2022).

3.4.3. Synthesis of Pt@g-C_3N_4/F-MWCNT

In order to synthesize Pt@g-C_3N_4/F-MWCNT nanocomposite, a well-known impregnation method has been utilized. In a typical synthesis method, a certain amount of MWCNT was added to 25 mL of water and sonicated for 1 h. Afterward, a certain amount of g-C_3N_4 was dispersed into the above solution, and 2.0 mL of H_2PtCl_6 (1000 ppm) was mixed at 100 °C for 4 h to obtain a suspension, and then freshly prepared $NaBH_4$ solution was added drop by drop to the solution under vigorous stirring at 80 °C over 10 h. Finally, the obtained

composite was rinsed three times with ethanol and water to take out the unreacted chemical species.

3.5. Preparation of TNF Imprinted Sensor

Initially, 1.5 mg mL^{-1} of Pt@g-C_3N_4/F-MWCNTs solution was dispersed in 1.0 mL deionized water and sonicated until a uniform Pt@g-C_3N_4/F-MWCNTs dispersion was obtained. Afterward, 8.0 μL of Pt@g-C_3N_4/F-MWCNTs nanocomposite was modified onto the screen-printed carbon electrode (SPCE). To remove any unattached nanocomposite from the surface, the as-fabricated electrode was washed with deionized water. The electropolymerization approach was utilized as an easy-to-implement polymer deposition and integration method. Compared to other methods, it can regulate the thickness and the density of the polymer layer through polymerization conditions. Then, the TNF imprinted surface on Pt@g-C_3N_4/F-MWCNTs (MIP/Pt@g-C_3N_4/F-MWCNTs/SPCE) was achieved by conducting 25 subsequent cyclic voltammetric (CVs) in the presence of 90.0 mM 2-Aminophenol in 0.1 M B-R(optimized) at a pH value of 5.0 including 30.0 mM TNF at a potential scan rate of 50.0 mV s^{-1}. In the inner Wall of MIP cavities, the amine and hydroxyl functional groups of TNF and 2-AP can interact using hydrogen bonding and π-π stacking, affecting the orientation of interfacial chemical functions cavities-template and the size conformity between imprinted cavity and template. Therefore, the specific cavities toward the template might be prepared after leaching. The cyclic voltammogram indicated an anodic peak at 0.4 V that can be assigned to the oxidation 2-AP. For control conditions, the TNF non-imprinted surface (NIP) was prepared under identical experimental details in the absence of TNF. After the electropolymerization, the composite membrane modified-electrode was rinsed with 1.0 mol L^{-1} HNO_3 at 400 rpm for 5.0 min to remove the TNF template. After the above treatment, the obtained MIP/Pt@g-C_3N_4/F-MWCNTs/SPCE possessed the ability to adsorb the target due to the specific hole formed on the membrane. Afterward, the imprinted electrode was washed with ethanol and ultrapure water and subsequently dried at room temperature. The illustration of the fabrication process of MIP/Pt@g-C_3N_4/F-MWCNTs/SPCE is provided in Fig. 3.1.

3.6.Determination Procedure

The constructed electrode was immersed in TNF-containing solutions (pH = 5.0) for 25 seconds while stirring (400 rpm) to detect TNF concentration. The electrode was then immersed in the cleaning solution (water with a neutral pH) for 5 seconds. Finally, the electrode was put in an electrochemical cell containing 10 mL of HCl (1.0 mol L^{-1}) to reduce the recognized target analytes, and then the DPV technique was performed. The obtained current signal was saved and employed to calculate the TNF amount in the previously established calibration curve solution.

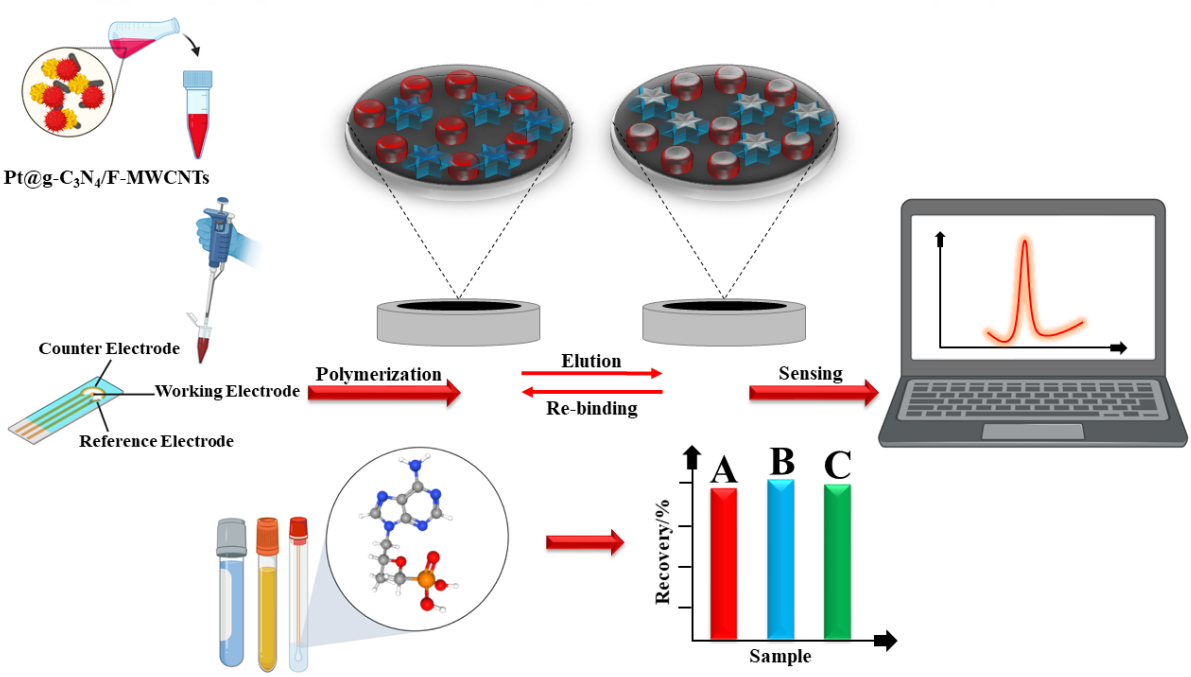

Figure 3.1. Schematic illustration of the TNF determination's preparation, modification, and analytical procedure of MIP/Pt@g-C_3N_4/F-MWCNTs/SPCE.

4. DISCUSSION

The extensive use of TNF for medical purposes needs the development of a reliable, sensitive, and quick approach for detecting TNF in actual samples with maximal therapeutic efficacy and minimal toxicities. To minimize its negative side effects and manage its concentration, an accurate and cost-effective quantitative measurement of TNF in biological fluids using a validated analytical technique is required. So far, different approaches have been used to quantify TNF in pharmaceutical dosage forms and biological material. For example, Kandagal et al. developed a straightforward reverse-phase high-performance liquid chromatographic method for TNF determination in pharmaceutical formulations and human plasma samples (Kandagal ve ark., 2008). MIP-based sensors represent a very interesting affinity reagent with potential application in diagnostics, rivaling normal sensors due to several advantages, mainly deriving from their chemical synthesis. In this thesis, the suitability of MIP on electrode surfaces for TNF detection was investigated. For this purpose, a well-described and studied monomer was chosen as a model system for biosensor development and polymerization. The standard curve showed a wide linear concentration range of 0.2–10 μg/ml (R^2=0.9966). Moreover, Nevase et al. proposed a simple, quick, and accurate spectrophotometric method for TNF quantitative estimation in bulk and tablet (Nevase ve ark., 2011). Dissolved TNF in methanol demonstrates absorption at about 260.0 nm, and the method obeys Beer's law at the concentration range of 10-100 μg/mL. Finally, this approach showed a satisfactory recovery.

Despite the reliability and selectivity of the aforementioned methods, these approaches are usually intricate, necessitating expensive instruments and manual operations, such as adjusting chromatographic settings and pre-treatment of HPLC samples. Recently, researchers have paid more attention to electrochemical approaches to address the obstacles of the traditional methods due to their ease of use, sensitivity, simple operation, lower reagent consumption, versatility, rapid response miniaturization, and the possibility of improving their selectivity and specificity using developing electrode surface by conductive nanocomposite (Deroco ve ark., 2018). However, because many interferents are present during real sample

analysis, selectivity is an inherent limitation in sensor performance, and restricting their use while extending the electrode surface can address this problem.

5. RESULTS

5.1. Optimization

Various contributing parameters, including the number of cycles for electropolymerization of 2-AP, the monomer/template molar ratio, elution duration, and electrolyte pH, were explored using differential pulse voltammetry (DPV) to produce an efficient MIP sensor with the most outstanding analytical performance. The optimization parameters used to synthesize MIP-nanocomposite briefly revealed a monomer/template ratio of 1:3, electro-polymerization cycles of 25, and a template elution time of 15 minutes in 1.0 mol L^{-1} HNO_3 with mild stirring resulted in better sensing performance. All studied parameters were considered independent. Fig. 5.1.A shows a visible oxidation peak at +0.7 V, showing that TNF molecules were successfully imprinted onto the electrode surface. However, as predicted, non-oxidation peaks are found during electropolymerization in the absence of TNF. In both cases, the current peaks dropped as the cycle number increased from the 1^{st} to the 25^{th}, indicating that the imprinted compact polymeric layer was effectively formed on the electrode surface.

5.1.1. Optimization of Physical Conditions

5.1.1.1. Effect of Monomer/Template Ratio

The monomer-to-template ratio of MIP film influences sensor sensitivity and reaction time to template molecules. It is difficult to properly polymerize when the ratio of template molecule to functional monomer is quite low. Additionally, if there are too many functional monomers, the template molecule may get entrenched and be difficult to remove. Also, the peak current and sensitivity are decreased. By comparing the DPV response of TNF on the produced electrode, the influence of the mole ratio of the monomer 2-AP to the template TNF was examined. As shown in Fig. 5.1.B, the peak current increased as the molar ratio of the monomer

to the template increased from 1:2 to 1:3 because of an increase in the number of imprinted sites. When the monomer/template ratios were less than 1:3, the inadequate amount of the monomer resulted in the lack of crosslinker and lowered peak current response, suggesting that the template molecules couldn't be adequately integrated with functional monomer pores. However, peak currents reduced when the molar ratio enhanced from 1:3 to 1:6; owing to the imprinted sites being covered by the excess of 2-AP, the effective imprinted sites decreased. Therefore, the molar ratio of the monomer to the template of 1:3 was chosen as the best condition.

5.1.1.2. Number of Cycles

As illustrated in Fig. 5.1.C, the normalized response of the MIP/Pt@g-C_3N_4/F-MWCNTs/SPCE depends on the number of potential cycles, which is related to the thickness of the polymer matrix (the thickness of the film increases with increasing the scan cycles of electropolymerization) and influences the sensitivity and linearity response of the MIP sensor by affecting the number of imprinted cavities (S. Wang ve ark., 2018). As shown, the response of the developed electrode to 0.5 μM TNF increased as the number of cycles increased from 15 to 25. During the process, the number of binding sites (cavities) increased, and therefore, the sensitivity of the MIP/Pt@g-C_3N_4/F-MWCNTs/SPCE increased. However, the response of the developed electrode decreased as the number of cycles increased to 35 and 45. The reasonable explanation is that the TNF's permeability to the electrode's surface decreased as the thickness of the non-conductive MIP film increased.

5.1.1.3. Elution Time

Elution time is another critical factor in obtaining specific imprinted cavities that affect sensitivity. The duration of the elution step was optimized by carefully immersing the electrodes with a selected solvent of HNO_3. As shown in Fig. 5.1.D, the current response increased with the increase of the incubating time and reached a stable value at 15 min without any significant

damage to the film. With the extension of time above 15 min, the current response changed remarkably since the absorption reached equilibrium, indicating that the imprinted sites have been removed entirely. Hence, t = 15 min was selected as optimum working conditions.

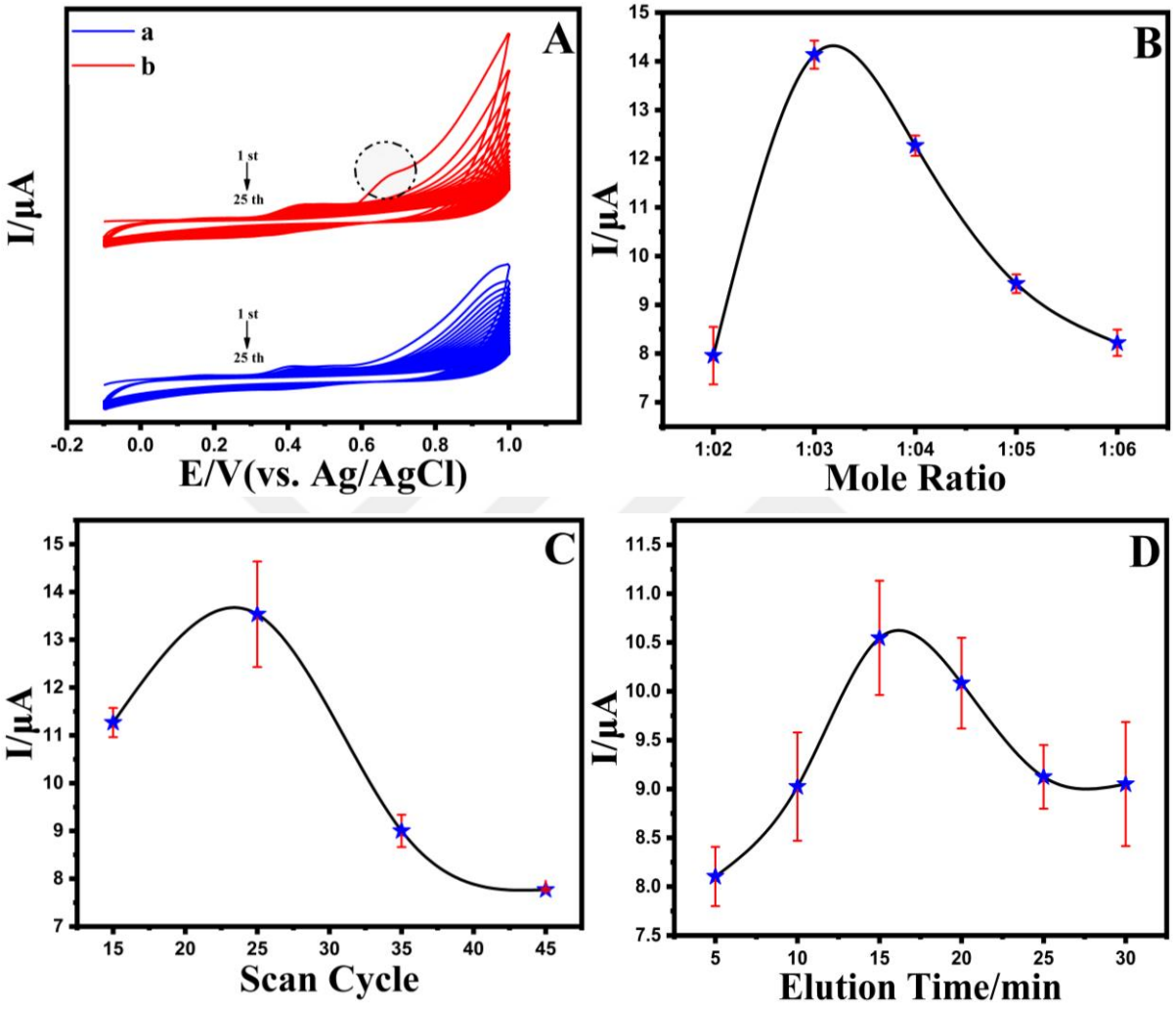

Figure 5.1. (A); CVs of 25 cycles of the electropolymerization onto MIP/Pt@g-C_3N_4/F-MWCNTs/SPCE (red curves) and NIP/Pt@g-C_3N_4/F-MWCNTs/SPCE (blue curves), the effect of the (B); mole ratio, (C); scan cycles, and (D); elution time on electrochemical response of TNF in 0.1 M B-R buffer.

5.2. Characterization of Pt@g-C_3N_4/F-MWCNTs

5.2.1. SEM analysis

The shape and morphology of the synthesized MIP-Pt@g-C_3N_4/F-MWCNTs before and after template removal were observed by SEM analyses. As can be seen, Fig. 5.2(A-D) indicates that the Pt nanoparticles are well-dispersed (average size of 50–100 nm) with F-MWCNTs and g-C_3N_4 nanosheets. Moreover, the SEM images show that g-C_3N_4 indicated a porous structure with few aggregations, and the tube-like F-MWCNTs have been interlinked effectively on the surface of the g-C_3N_4. However, the MIP-Pt@g-C_3N_4/F-MWCNTs indicate agglomeration structures. Furthermore, before template removal, a compact and rough surface was found in MIP-Pt@g-C_3N_4/F-MWCNTs owing to direct surface imprinting (Fig. 5.2 A and C), providing a large specific surface area for TNF identification.

Interestingly, after removing the TNF templates, the surface of the MIPs became rougher and more cavities were generated (Fig. 5.2 B and D), indicating that the MIP sensor had been synthesized, and the compact structure of MIP changed after the extraction process, and some cavities were observed on the surface related to the removal of TNF from MIP film. On the other hand, the cavities created in the leached polymer can be attributed to the template removal from polymer film after the process of leaching using HNO_3. It is worth mentioning that a rough electrode surface may have better sensitivity than a smooth surface due to increased surface area (L. Zhang ve ark., 2014).

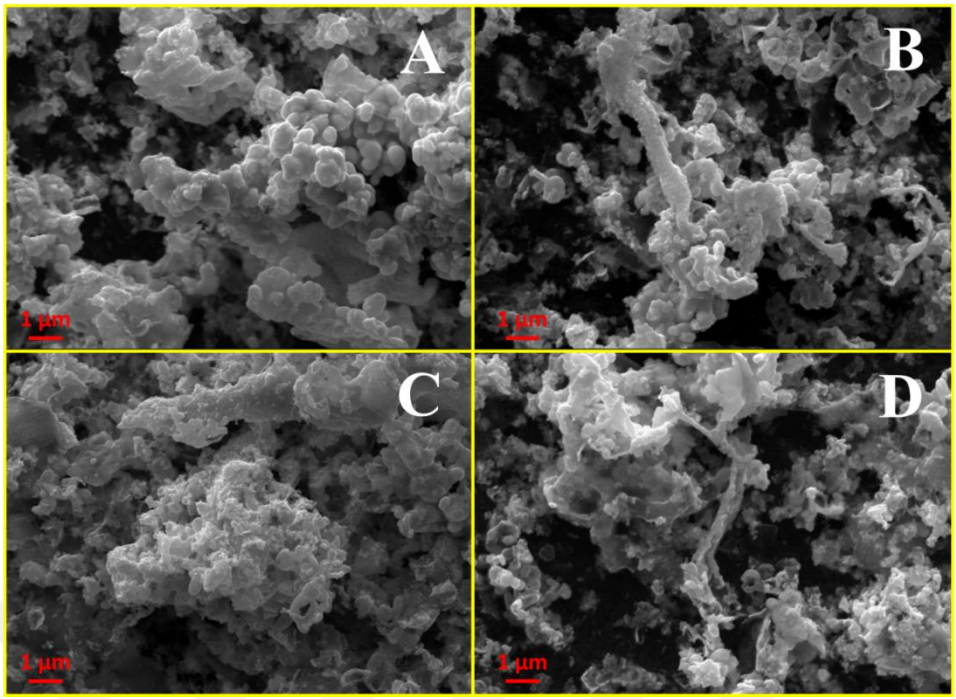

Figure 5.2. SEM images of MIP-Pt@g-C_3N_4/F-MWCNTs (A,C); before template removal and (B,D); after template removal.

5.2.2. Elemental Mapping Analysis

The elemental distribution and composition of the Pt@g-C_3N_4/F-MWCNTs nanocomposite were analyzed by elemental mapping analysis (Fig. 5.3). The results confirmes the dispersion of C, N, and Pt throughout the nanocomposite.

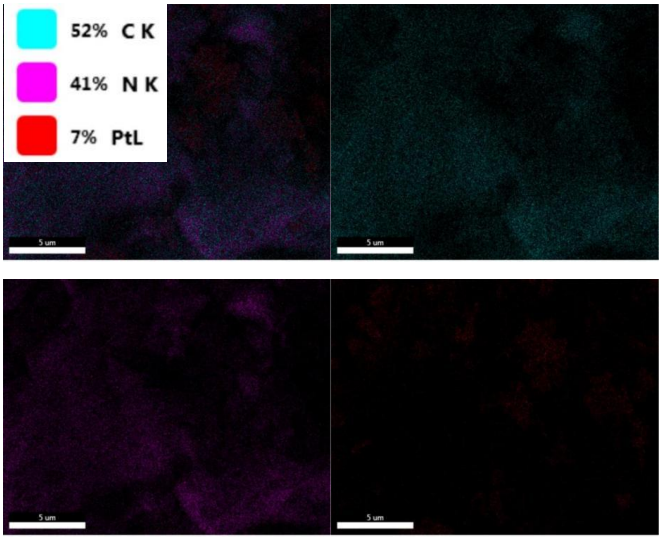

Figure 5.3. Elemental mapping of Pt@g-C_3N_4/F-MWCNTs nanocomposite.

5.2.3. EDX Analysis

The EDX pattern of Pt@g-C_3N_4/F-MWCNTs indicates the presence of Pt, N, and C elements with the elemental percentage of 12.67, 56.93, and 30.41%, respectively, confirming that the synthesis of Pt@g-C_3N_4/F-MWCNTs has been performed successfully (Fig. 5.4).

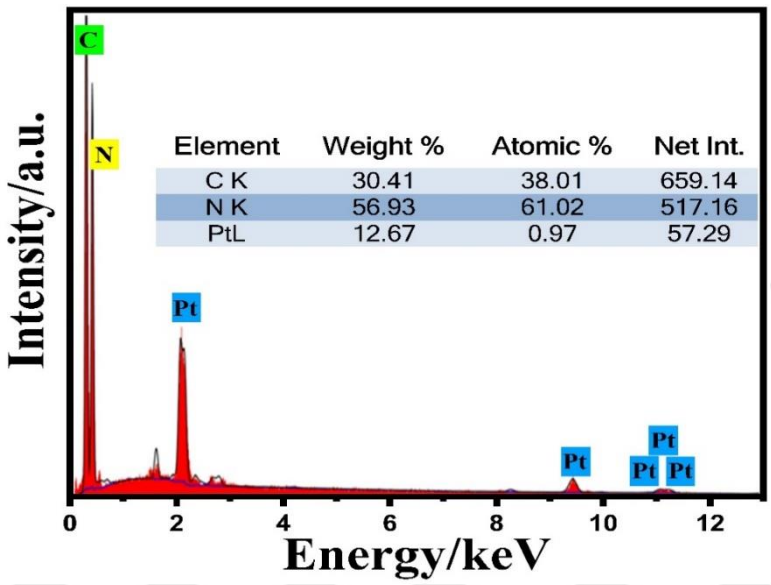

Figure 5.4. EDX of Pt@g-C_3N_4/F-MWCNTs nanocomposite.

5.2.4. XRD Analysis

The XRD patterns show that the MIP-Pt@g-C_3N_4/F-MWCNTs nanocomposites have been successfully synthesized (Fig. 5.5). The typical diffraction peaks of g-C_3N_4 can be seen in Fig. 2A at 27.5° and 13.0°, which is attributed to aromatic segment stacking (Gebreslassie ve ark., 2019). Moreover, the MWCNT pattern at 26.5° and 43.2° may be attributed to its (002) and (101) crystal planes, showing that MWCNTs have high crystallinity. However, despite leading the characteristic peaks of MWCNTs and g-C_3N_4 in the Pt@g-C_3N_4/F-MWCNTs nanocomposites, they are absent in the MIP-Pt@g-C_3N_4/F-MWCNTs nanocomposites, which could be attributed to several reasons, including the low concentration of MWCNTs and high dispersion in the samples and coating of these materials using molecularly imprinted polymers, which indicates successful synthesis. Furthermore, the diffraction peaks observed of 39.9, 45.7, 69.6, and 82.6° were assigned to reflexes of (111), (200), (220), and (311) of planes of a face-centered platinum cell, respectively (Kasturi ve ark., 2020; Li ve ark., 2009), which are in good

agreement with the standard card of cubic Pt (JCPDS No. 4–802). The results clearly affirm a crystalline structure of the as-synthesized MIP-Pt@g-C_3N_4/F-MWCNTs. Besides, on comparing the XRD spectra of MIP-Pt@g-C_3N_4/F-MWCNTs and Pt@g-C_3N_4/F-MWCNTs, it was found that the band intensities increased and became sharp, possibly due to the effects of molecular imprinting on the electrodes.

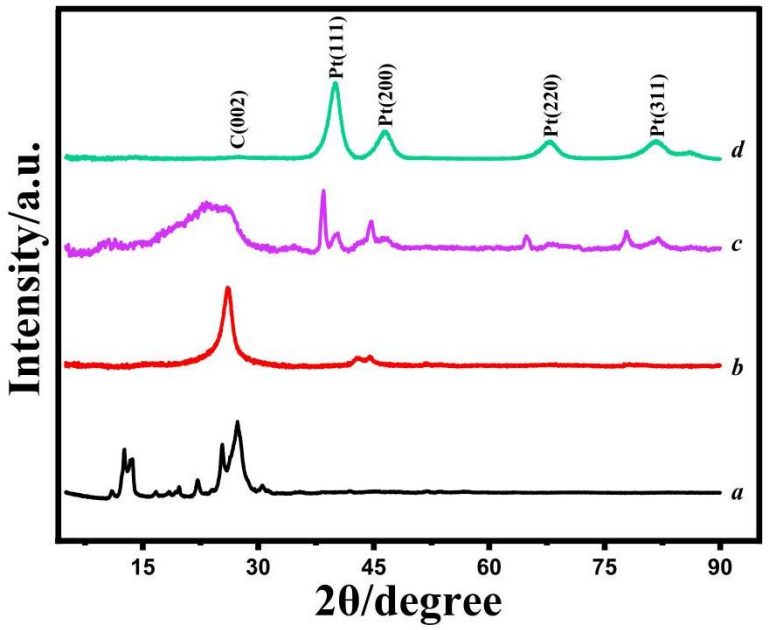

Figure 5.5. XRD patterns of g-C_3N_4 (a), F-MWCNT (b), Pt@g-C_3N_4/F-MWCNTs (c), and MIP-Pt@g-C_3N_4/F-MWCNTs (d).

5.2.5. FTIR Analysis

The chemical structure and bonding interaction of g-C_3N_4, F-MWCNTs, Pt@g-C_3N_4/F-MWCNTs, and MIP-Pt@g-C_3N_4/F-MWCNTs nanocomposite in the range of 400 to 4000 cm^{-1} were observed, and the result is shown in Fig. 5.6. The absorption band near 1636 cm^{-1} corresponded to C=N stretching, while the two bands at 1240 and 1321 cm^{-1} attributed to the characteristic stretching mode of aromatic CN heterocycles (Xu ve ark., 2013). Additionally, the sharp absorption band at 815 cm^{-1} was attributed to the breathing mode of triazine units (Zhao ve ark., 2014). The acid (single bond COOH) functionalization of MWCNT was also verified through peaks formed related to the existence of diverse functional groups absence in the MWCNTs. The MIP-Pt@g-C_3N_4/F-MWCNTs indicated the carbonyl bands (C=O) at

around 1733 cm^{-1}, which may form during polymerization (Ayerdurai ve ark., 2021; Kadivar ve Aliakbar, 2021). The strong stretching C-C bond was observed in the spectrum of wave number 1040 cm^{-1}. The strong peak formed at 3520 cm^{-1} confirmed the hydroxyl group's presence and demonstrated that acid treatment efficiently functionalized the MWCNTs. The strong peaks formed in the region of 1394 cm^{-1} obviously describe the stretching vibration of the ether (C-O) group. In addition, the peak at 452 cm^{-1} was due to the presence of Pt nanoparticles (Mahmoudian ve ark., 2020). As shown in Fig. 5.6 (d) for MIP- Pt@g-C_3N_4/F-MWCNTs, the main peaks of the nanocomposite were found to be similar, and only minor shifts in the position of the peaks were observed. Moreover, the broad peak of the O-H group at 3200-3700 cm^{-1} was diminished, confirming the complete synthesis of MIP-Pt@g-C_3N_4/F-MWCNTs. Furthermore, the characteristic absorbance band appeared at 2610 cm^{-1}, which is related to 2-AP (Kadivar ve Aliakbar, 2021). Therefore, the FT-IR spectra confirmed the successful synthesis of MIP-Pt@g-C_3N_4/F-MWCNTs and the presence of g-C_3N_4, Pt, and F-MWCNTs in the nanocomposite, while the reduction of Pt^{2+} to Pt^0 and the percentage of Pt was reaffirmed by the XRD and EDX results.

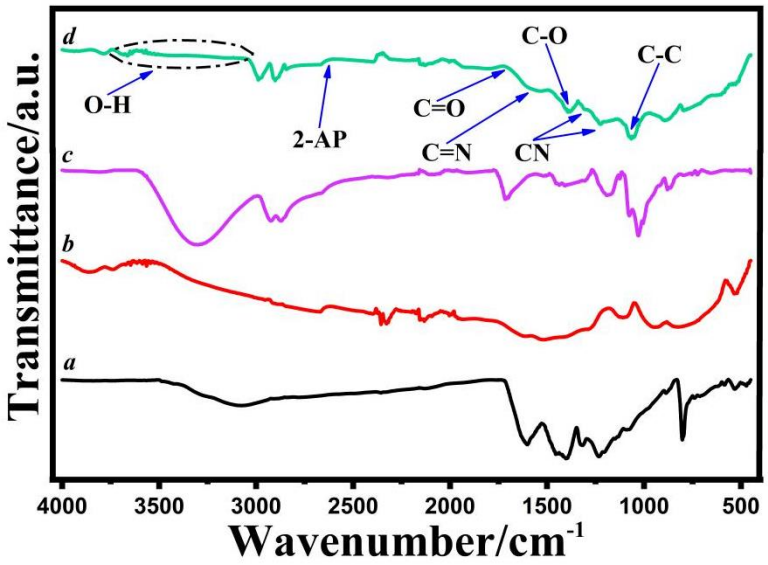

Figure 5.6. FT-IR spectra of g-C_3N_4 (a), F-MWCNT (b), Pt@g-C_3N_4/F-MWCNTs (c), and MIP-Pt@g-C_3N_4/F-MWCNTs (d).

5.2.6. AFM

AFM was used to study topography, which is related to the root mean square (RMS) roughness, for the MIP sensor during its preparation process. The presented AFM images show the 3D side view of the Pt@g-C_3N_4/F-MWCNTs (Fig. 5.7 A), MIP-Pt@g-C_3N_4/F-MWCNTs before template removal (Fig. 5.7 B) and MIP-Pt@g-C_3N_4/F-MWCNTs after template removal (Fig. 5.7 C). As shown in Fig. 5.7 A, the electrode has been homogeneously modified by Pt@g-C_3N_4/F-MWCNTs, with nanoparticles having an average of 300 nm of diameter and 30 nm of height, with RMS of 43.7 nm as well as with a uniform and smooth profile. Modifying the electrode with the polymeric layer during the molecular imprinting process resulted in a massive change in roughness. The RMS values obtained were 9.8 nm for MIP before removing the TNF and 38.35 nm for MIP after the removal. As you can see, after the template removal with acid treatment, the RMS roughness value of the surface increased, and the light-colored areas on 3D images were enlarged, thus indirectly confirming MIPs deposition on the Pt@g-C_3N_4/F-MWCNTs surface.

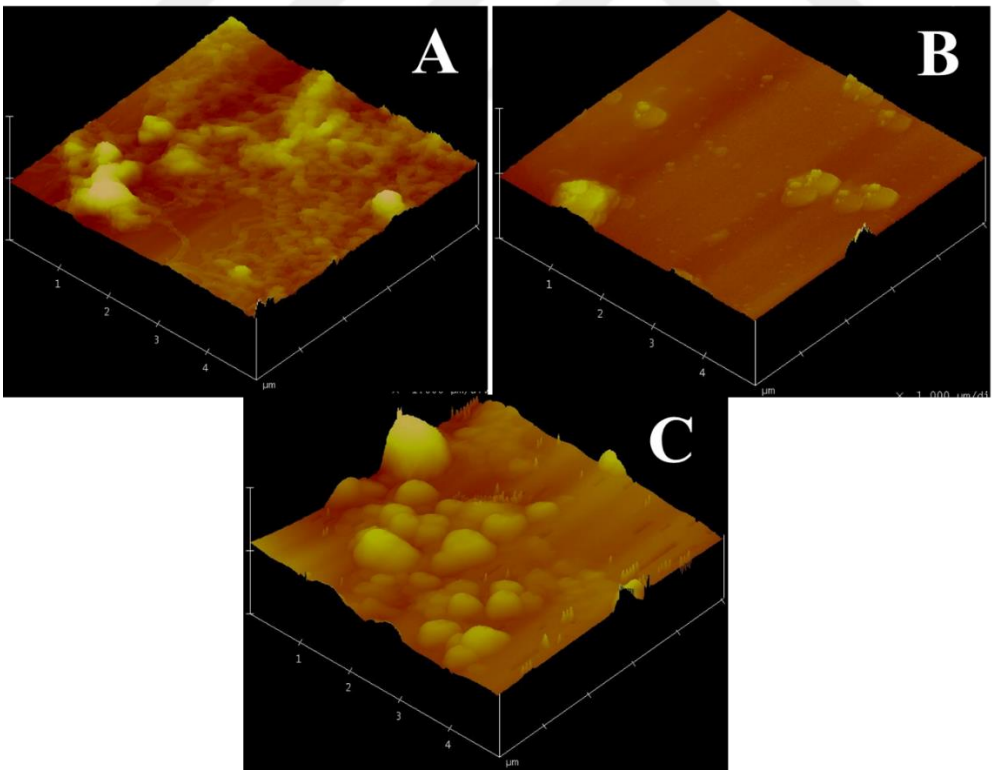

Figure 5.7. AFM images of (A); Pt@g-C_3N_4/F-MWCNTs, (B); MIP-Pt@g-C_3N_4/F-MWCNTs before template removal, and (C); MIP-Pt@g-C3N4/F-MWCNTs after template removal.

5.2.7. BET Analysis

Furthermore, to further understand the surface characteristics of the materials, BET analysis for MIP-Pt@g-C_3N_4/F-MWCNTs before and after template removal was used using a nitrogen adsorption characterization (Fig. 5.8). The curve comparison indicated that the nitrogen adsorption-desorption capacity of MIP-Pt@g-C_3N_4/F-MWCNTs after template removal is significantly greater than that of MIP-Pt@g-C_3N_4/F-MWCNTs before template removal, thereby suggesting that the imprinting site has been successfully formed.

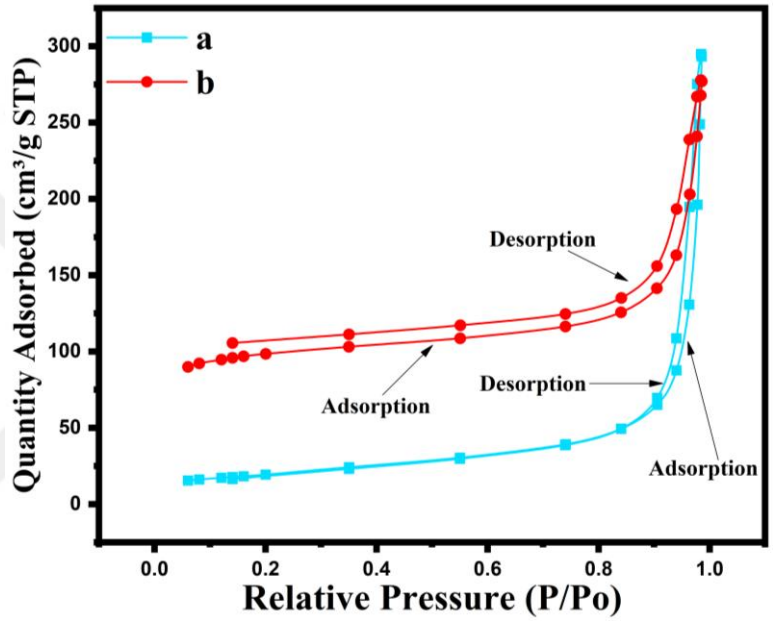

Figure 5.8. Nitrogen adsorption-desorption diagram of MIP-Pt@g-C_3N_4/F-MWCNTs before (a) and after (b) template removal.

5.2.8. Binding analysis of imprinted Pt@g-C_3N_4/F-MWCNTs

The TNF recognition ability of the MIP-Pt@g-C_3N_4/F-MWCNTs was investigated by the static absorption experiments in the presence of a mixture of 50.0 ppm TNF and 20.0 mg of MIP-Pt@g-C_3N_4/F-MWCNTs and NIP-Pt@g-C_3N_4/F-MWCNTs. After letting the dispersions for 5 min on a rocking table, the solutions were filtered and analyzed by UV-Vis. As shown in Fig. 5.9, the maximum absorption wavelength of TNF (in the absence of MIP and NIP composite) at about 250 nm was significantly decreased when 20.0 mg of MIP-Pt@g-C_3N_4/F-

MWCNTs (after template removal) was added as the absorber, attributing an increasing filling of MIP free sites for each enhance of TNF concentration. On the other hand, the absorption test indicated that the MIP-Pt@g-C_3N_4/F-MWCNTs have a specific binding capacity for the template molecule. Moreover, these spectra gradually decreased and fixed after 30 minutes, meaning that all MIP-Pt@g-C_3N_4/F-MWCNTs sites have been filled by TNF molecules. Interestingly, when 20.0 mg of NIP-Pt@g-C_3N_4/F-MWCNTs was added to 50.0 ppm TNF, compared to MIP-composite, the absorption wavelength of the NIP-composite changed little because the NIP-composite does not add template molecules in the synthesis, so it is unable to form imprinted holes that match the structure and function of template molecules. It has no specific recognition function for TNF molecules, and the sensor's sensitivity is significantly reduced. Therefore, this study further confirmed that the MIP layer possessed many special recognition cavities for TNF, and the MIP-Pt@g-C_3N_4/F-MWCNTs can be utilized for rapid and selective detection of TNF because a large number of binding sites were existent.

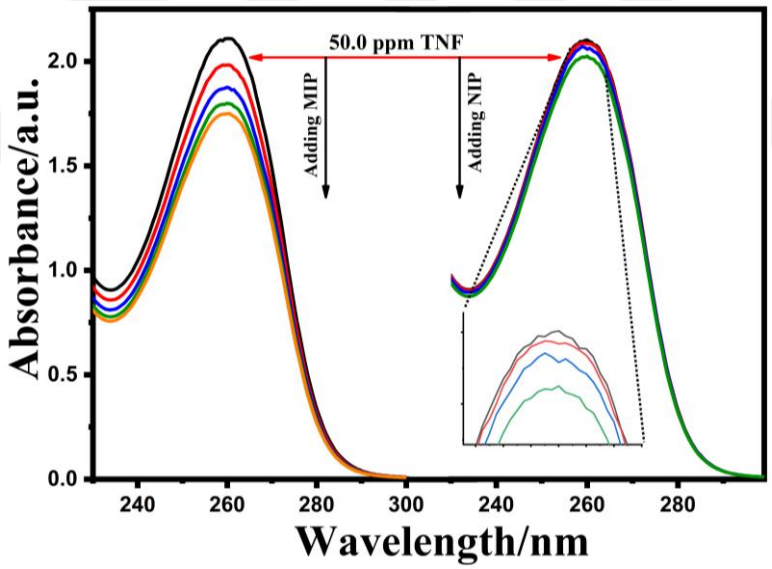

Figure 5.9. UV-Vis spectra of 50.0 ppm TNF in the presence of MIP-Pt@g-C_3N_4/F-MWCNTs and NIP-Pt@g-C_3N_4/F-MWCNTs.

In addition, chemical bond analysis was performed using molecular dynamics simulation to confirm the binding between monomer and template. As shown in Fig. 5.10 A, the optimized structure indicated the TNF-imprinted binding site in the MIP polymer. The

specific hydrogen bonding and π-π stacking among the 2-AP and TNF are responsible for the selective binding behavior. Based on calculations obtained from the highest occupied molecular orbital (HOMO) and lowest unoccupied molecular orbital (LUMO), electrostatic, electron density states, and atomic charge of molecules, the interaction between TNF and 2-AP followed by a 2-aminophenol polymer was investigated using Materials Studio 2017 software (Fig. 5.10 B). The difference between HOMO and LUMO energy for TNF and 2-AP was -0.1408 eV and -0.1433 eV, respectively. As can be seen, the difference in HOMO and LUMO energy is less for 2-AP, so it is more reactive than TNF, approving a high binding ability of the MIP structure to the target TNF. Moreover, when tenofovir interacts with 2-AP polymer, the system becomes stable; the total energy and adsorption energy results, which are -360.044 and -731.477 Kcal/mol, confirm these results. Furthermore, molecular dynamics with a time of 100 ns were studied to investigate the type of interactions, after which the system was balanced and the energies were fixed. As the results show, the interactions between TNF and the 2-AP polymer were van der Waals type, an electrostatic type, and most of its van der Waals reactions are of the hydrogen bond type. Therefore, the 2-AP polymer can be well used to absorb TNF in the molecularly imprinted polymer.

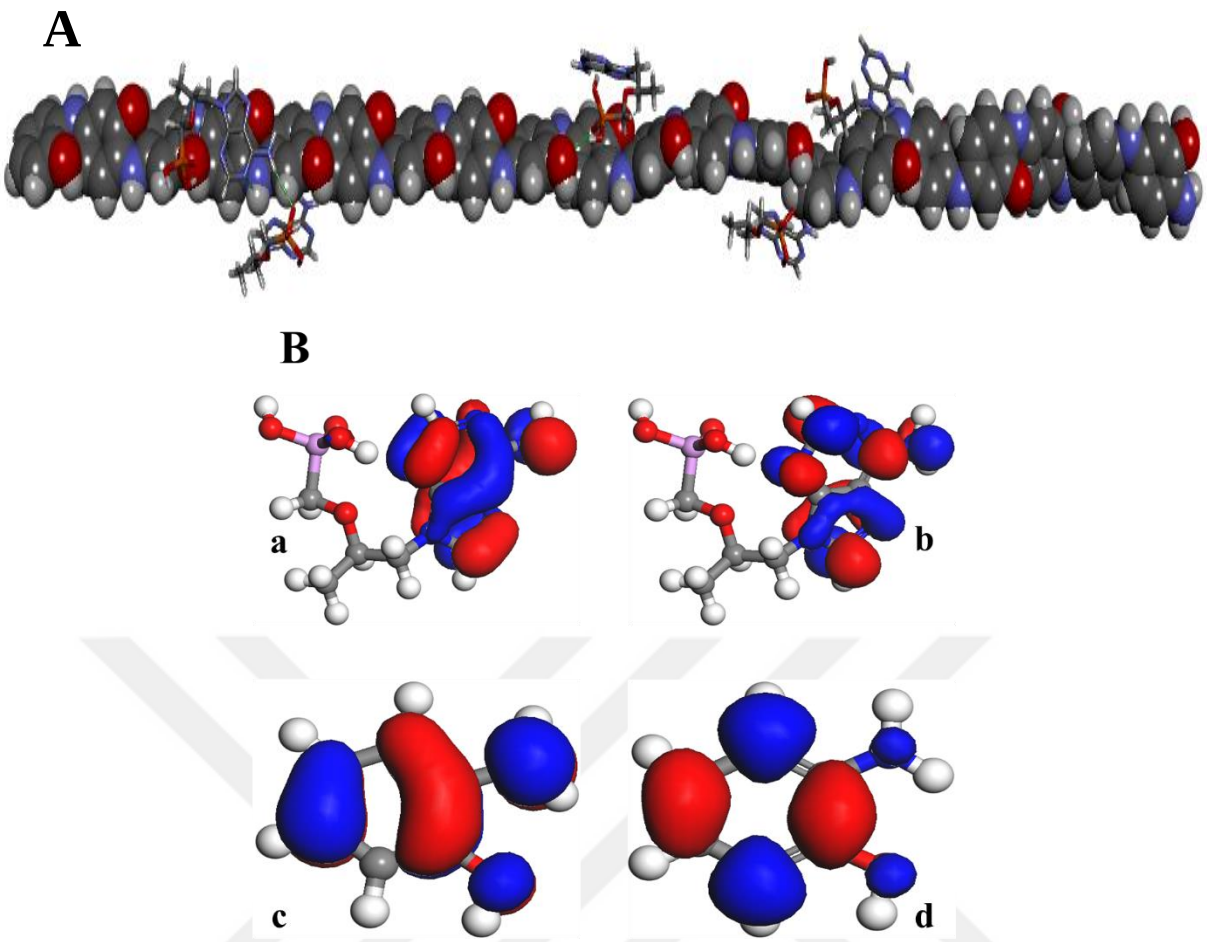

Figure 5.10. (A); Interaction and bond length between TNF and 2-AP polymer after molecular dynamics in Materials Studio 2017 software, (B); Different forms of a) HOMO TNF, b) LUMO TNF, c) HOMO 2-AP, and d) LUMO 2-AP in Materials Studio 2017 software.

5.3. Sensor Characterization

5.3.1. Electrochemical Characteristics of Unmodified and Modified Electrodes

Electrocatalytic active surface area peak to peak separation and interface characteristics of bare SPCE, NIP-Pt@g-C_3N_4/F-MWCNTs/SPCE, MIP-Pt@g-C_3N_4/F-MWCNTs/SPCE before template removal, and MIP-Pt@g-C_3N_4/F-MWCNTs/SPE after template removal were investigated through CVs in the presence of 5.0 mM $[Fe(CN)_6]^{3-/4-}$ containing 0.1 M KCl. The peak-to-peak separation (ΔEp) value among anodic and cathodic currents was observed. The ΔEp value of MIP-Pt@g-C_3N_4/F-MWCNTs/SPCE after template removal (ΔEp = 161 mV) was

lower than that of the bare SPCE (ΔEp = 186 mV), as shown in Fig. 5.11, suggesting quicker electron transfer and more active sites compared to other electrodes. Furthermore, an improvement in both anodic and cathodic currents has clearly demonstrated the considerable electrocatalytic activity of MIP-Pt@g-C_3N_4/F-MWCNTs/SPCE after template removal, indicating the removal of the template-produced cavities in the polymeric matrix, therefore enhancing the porosity and increasing the diffusion of $[Fe(CN)_6]^{3-/4-}$ and the redox reaction on the electrode surface. Moreover, the CV peak of MIP-Pt@g-C_3N_4/F-MWCNTs/SPCE before template removal was significantly lower than that of MIP-Pt@g-C_3N_4/F-MWCNTs/SPCE after template removal, indicating that MIP-Pt@g-C_3N_4/F-MWCNTs/SPCE covered with the polymer film has low conductivity, hindering the direct redox reaction of $[Fe(CN)_6]^{3-/4-}$ and prevents most of $[Fe(CN)_6]^{3-/4-}$ from passing through the polymer film towards the electrode surface. As expected, NIP-Pt@g-C_3N_4/F-MWCNTs/SPCE showed a lower electrochemical response than MIP-Pt@g-C_3N_4/F-MWCNTs/SPCE because the polymeric matrix blocks the electrode surface. It is also consistent with the FT-IR, XRD, AFM, BET, and SEM characterization results. Therefore, MIP-Pt@g-C_3N_4/F-MWCNTs/SPCE has been chosen for further experiments.

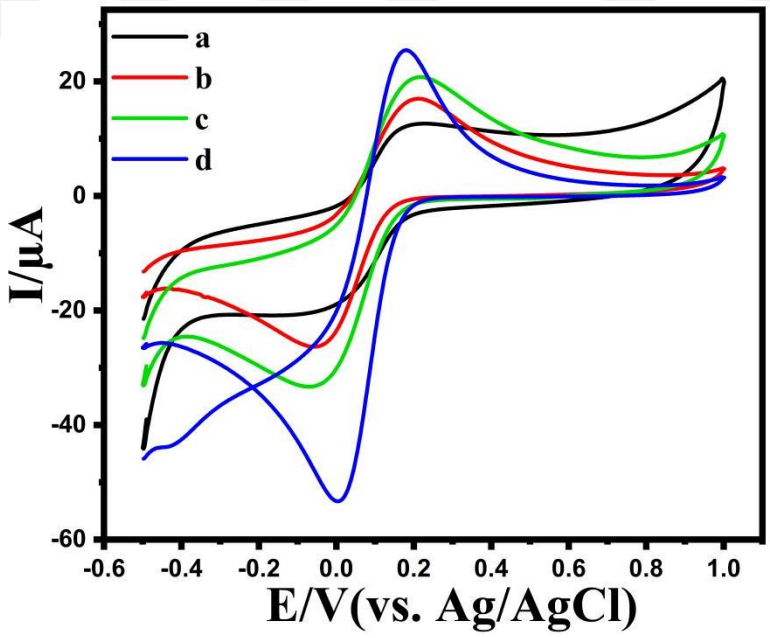

Figure 5.11. CVs of 5.0 mM $[Fe(CN)_6]^{3-/4-}$ containing 0.1 M KCl at bare electrode (a), g-C_3N_4/SPCE, and Pt@g-C_3N_4/F-MWCNTs/SPCE.

Moreover, electrochemical impedance spectroscopy (EIS) is one of the most important electrochemical methods. The Nyquist plots exhibited that the charge transfer modified electrodes in the 5.0 mM $[Fe(CN)_6]^{3-/4-}$ containing 0.1 M KCl. As illustrated in Fig. 5.12, both the MIP before template removal and NIP electrodes indicated the appearance of a high-frequency semicircle which shows the $[Fe(CN)_6]^{3-/4-}$ electrode reaction. The treatment remarkably enhanced the electron transfer rate between the solution and the electrode due to removing the unstable monomers on film, indicating the successful extraction of TNF from the imprinted polymer. MIP-Pt@g-C_3N_4/F-MWCNTs/SPCE after template removal demonstrated an electrode process about two times faster than NIP-Pt@g-C_3N_4/F-MWCNTs/SPCE. These results confirm that MIP-Pt@g-C_3N_4/F-MWCNTs increased the developed electrode's conductivity and electro-active surface area.

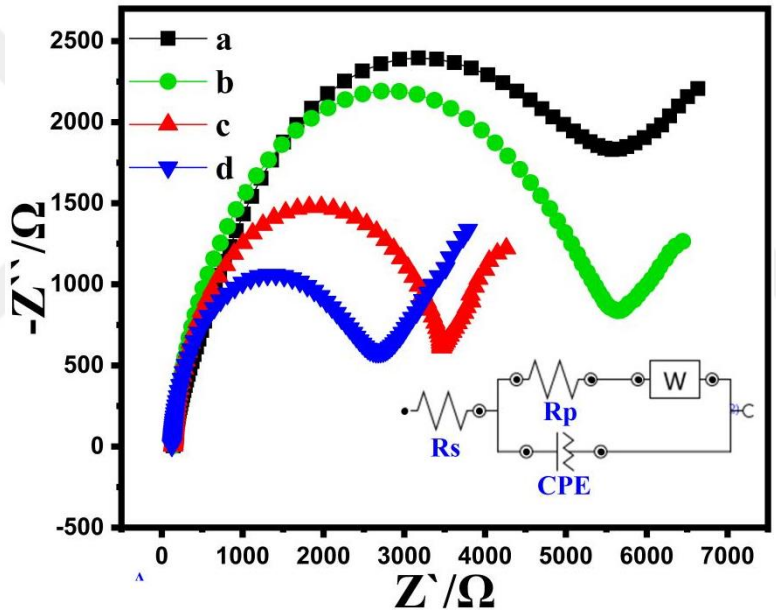

Figure 5.12. EIS of 5.0 mM $[Fe(CN)_6]^{-3/-4}$ containing 0.1 M KCl at bare electrode (a), g-C_3N_4/SPCE, and Pt@g-C_3N_4/F-MWCNTs/SPCE.

5.3.2. Electro-active Surface Area

The surface modification of the SPCE with the produced composite was confirmed by utilizing the Randles-Sevcik equation (Eq. 5.1) to calculate its electroactive surface area. (Fig. 5.13):

$$I_{pa} = 2.69 \times 10^5 AC n^{3/2} D^{1/2} v^{1/2} \quad \text{(Eq. 5.1)}$$

Where I_{pa} is the electroactive substance's peak current, A is the sensor's electroactive surface area, C is the probe molecule's molar concentration, n is the number of transferred electrons in the electrochemical reaction, D is the redox probe molecule's diffusion coefficient (D=7.26 10^{-6} cm^2 s^{-1}), and *v* shows the scan rate. The electroactive areas for bare SPCE, NIP-Pt@g-C_3N_4/F-MWCNTs/SPCE, MIP-Pt@g-C_3N_4/F-MWCNTs/SPCE before elution and MIP-Pt@g-C_3N_4/F-MWCNTs/SPCE after elution were found to be 0.0746, 0.2287, 0.2449, and 0.4721 cm^2, respectively, which presented a 6.32 times larger area than that of the bare SPCE owing to its abundant active sites. According to these findings, the MIP-Pt@g-C_3N_4/F-MWCNTs/SPCE composite has the highest electro-active surface area for electron transport between the redox probe and the working electrode, which was consistent with the results of CV and EIS, and the electroactive area increased after the template removal, which further proved the successful synthesis of MIP-Pt@g-C_3N_4/F-MWCNTs/SPCE.

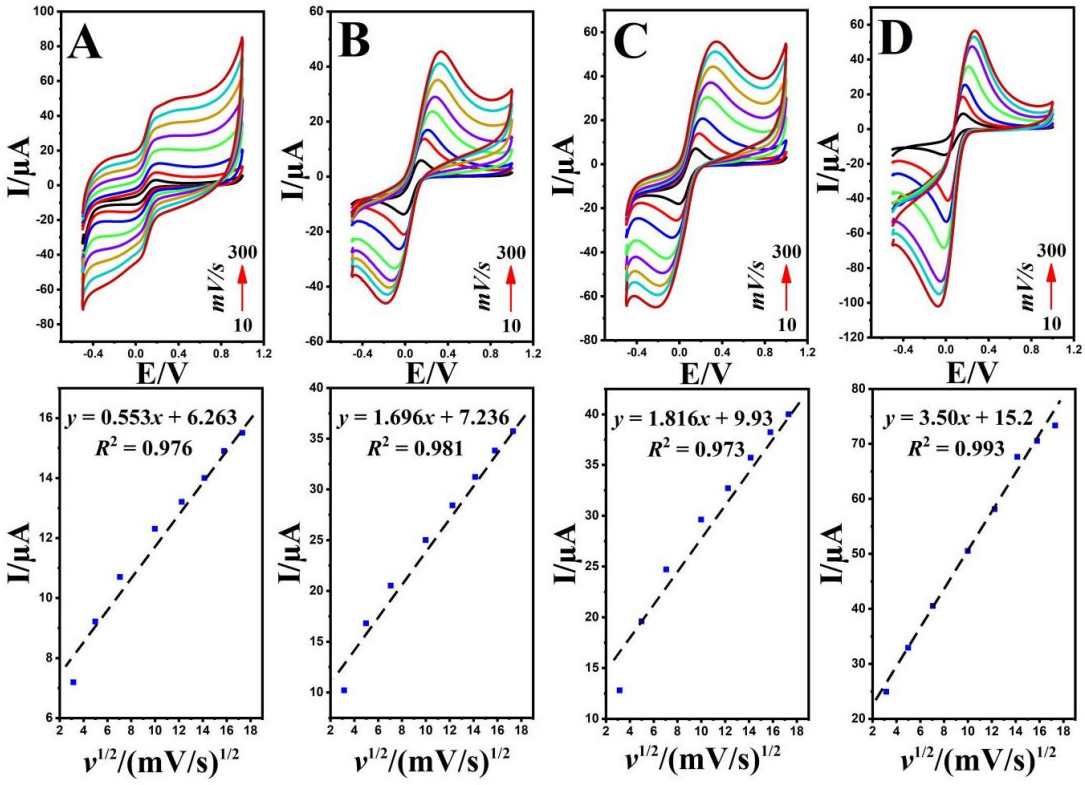

Figure 5.13. CVs of 5.0 mM $[Fe(CN)_6]^{3-/4-}$ in 0.1 M KCl at (A); bare electrode, (B); NIP-Pt@g-C_3N_4/F-MWCNTs/SPCE, (C); MIP-Pt@g-C_3N_4/F-MWCNTs/SPCE before template removal, (D); MIP-Pt@g-C_3N_4/F-MWCNTs/SPCE after template removal.

5.3.3. Electrochemical Behavior of TNF

In order to assess the influence of MIP, the DPV curves of TNF at various modified electrodes were observed in the presence of 0.5 μM TNF, as shown in Fig. 5.14. After rebinding, NIP/SPE and MIP/SPCE demonstrated low oxidation peaks (Fig. 5.14 A), while the various type of Pt@g-C_3N_4/F-MWCNTs/SPCE exhibited a more significant peak, as illustrated in Fig. 5.14 B. On the other hand, the oxidation current of the antiviral agent TNF was improved by modifying the electrodes. The oxidation currents of the developed electrode (MIP-Pt@g-C_3N_4/F-MWCNTs/SPCE) dramatically increased (4.14 to 11.2 μA), indicating that the MIP has higher adsorption to TNF. Moreover, The resulting voltammetric curves presented by DPV illustrated that the modification of SPCE surfaces by Pt@g-C_3N_4/F-MWCNTs/SPCE remarkably increased the sensitivity towards the TNF with a superior electrocatalytic activity (i.e., from 1232 to 1208 mV) compared to that of bare SPCE owing to their large active surface areas and synergic effects between Pt NPs, g-C_3N_4, and F-MWCNTs. Compared with the NIP-based electrode, the MIP-based electrode, after removing, showed improved peak current response and a change in the oxidation potential, confirming the effective active sites that existed in the MIP membrane. The developed electrode effectively supplied many binding sites and accelerated the adsorption of imprinted molecules, significantly improving detection efficiency. Moreover, the remarkable enrichment of TNF at MIP-Pt@g-C_3N_4/F-MWCNTs/SPCE was obviously observed compared to a bare SPCE, indicating that the π–π interaction between MIP-Pt@g-C_3N_4/F-MWCNTs/SPCE. However, the peak signal at MIP-Pt@g-C_3N_4/F-MWCNTs/SPCE was smaller than at Pt@g-C_3N_4/F-MWCNTs/SPCE, suggesting that the MIP film blocked the electron transfer of TNF to some extent, probably because of the hindrance of the polymer. The results confirm the high conductivity of MIP/Pt@g-C_3N_4/F-MWCNTs/SPCE and large active surface area compared to other modified SPE and bare SPCE.

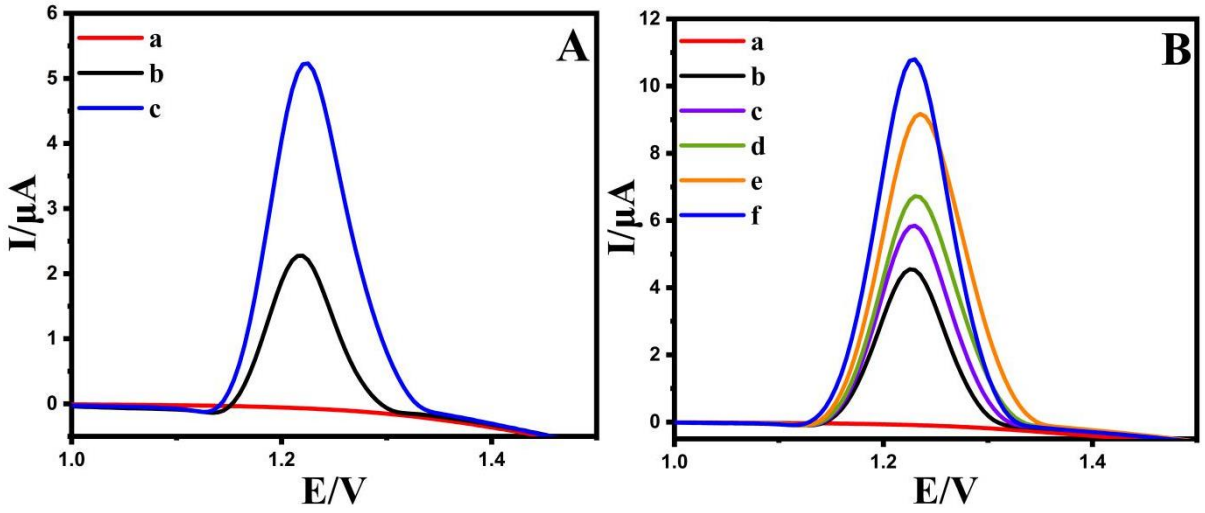

Figure 5.14. (A); DPVs of (a) MIP/SPCE in blank buffer solution, (b) NIP/SPCE after rebinding, and (c) MIP/SPCE after rebinding, (B); DPVs of (a) MIP/Pt@g-C_3N_4/F-MWCNTs/SPCE in blank buffer solution, (b) bare SPCE, (c) NIP/Pt@g-C_3N_4/F-MWCNTs/SPCE; (d) F-MWCNT/SPCE; (e) g-C_3N_4/F-MWCNT/SPCE, (f) Pt@g-C_3N_4/F-MWCNTs/SPCE in the presence of 0.5 μM TNF containing 0.1 M BR buffer at pH 5.0.

5.3.4. pH Study

The influence of the buffer pH on the oxidation potential and current of TNF was investigated over the pH range between 3.0 and 9.0 by the DPV method on MIP-Pt@g-C_3N_4/F-MWCNTs/SPCE using Britton-Robinson buffer (Fig. 5.15). As can be seen, the peak oxidation potential of TNF shifted to negative values with an increase in pH, confirming that electro-oxidation of TNF is relative to proton exchange and the current oxidation peak and potential of TNF depend on the pH value. The highest sensitivity oxidation current was determined at pH 5.0. Therefore pH 5.0 was selected as the best pH value. Moreover, Fig. 5.13 (inset) indicates the plots of the oxidation potential of TNF vs. pH. A decreasing trend can be observed at E_{pa}=-0.05 pH+1.51 (R^2=0.984), and this slope (0.05 E_{pa}/pH) is near to the theoretical value (0.059 E_{pa}/pH), suggesting that the number of protons and electrons in the electro-oxidation of TNF are equal (Festinger ve ark., 2022). According to the results, Fig. 5.16 was presented for the mechanism of electro-oxidation of TNF on the MIP-Pt@g-C_3N_4/F-MWCNTs/SPCE.

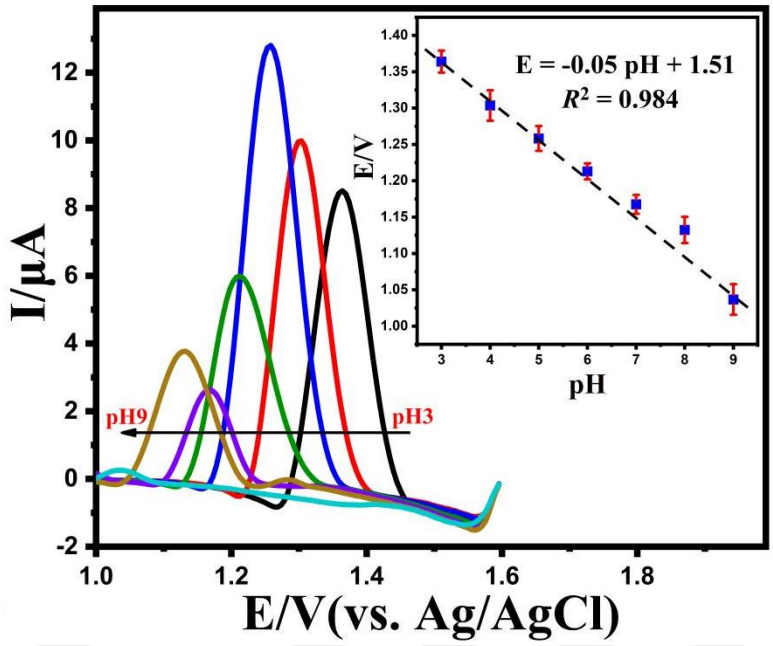

Figure 5.15. DPVs of 0.5 μM TNF at diverse pH (3.0 to 5.0) on MIP/Pt@g-C_3N_4/F-MWCNTs/SPCE surface.

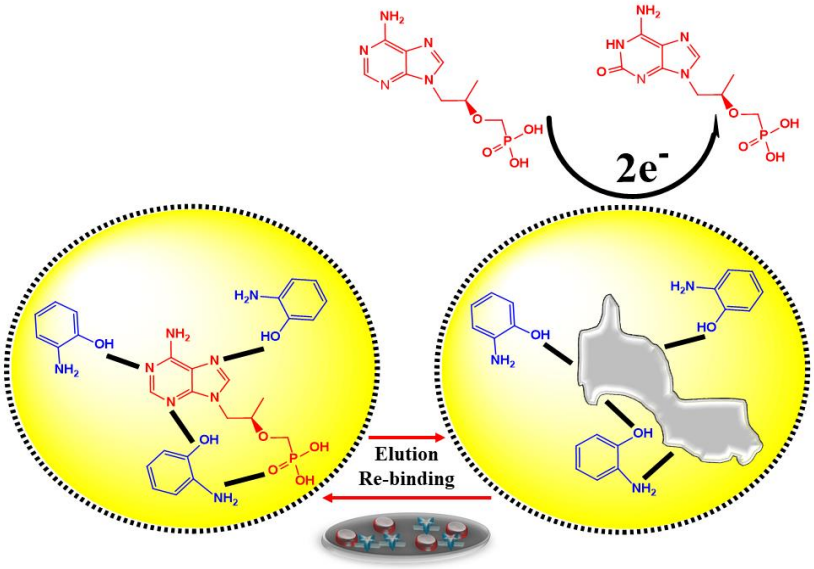

Figure 5.16. Electrochemical mechanism of TNF towards MIP-Pt@g-C_3N_4/F-MWCNTs/SPCE.

5.3.5. Scan Rate Study

The influences of the scan rate were also studied in the range of 10.0 to 500.0 mV/s on MIP-Pt@g-C_3N_4/F-MWCNTs/SPVEin the presence of 0.5 µM TNF in 0.1 M B-R buffer at pH 5.0 (Fig. 5.17). With the increase of the scan rate, the intensities of currents also increased. The plot of peak current (I_{pa}) vs. the square root of scan rate ($v^{1/2}$) was also plotted to be linear in the range 10.0–500.0 mVs^{-1} (I_{pa}=0.711$v^{1/2}$- 2.28, (R^2=0.991)), indicating that the process of TNF at the modified electrode is diffusion-controlled (Karimi-Maleh ve Arotiba, 2020). Furthermore, the catalytic oxidation peak potential moves dramatically to the positive side as the scan rate increases, suggesting a kinetic constraint in the interaction between the modified electrode's oxidation site and the analyte and also exhibits that the electrode reaction of TNF on MIP-Pt@g-C_3N_4/F-MWCNTs/SPCE is irreversible.

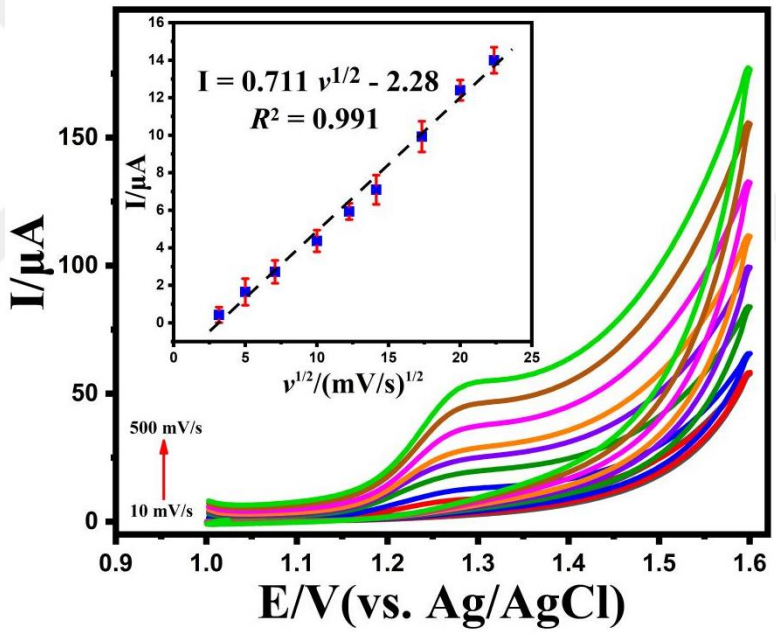

Figure 5.17. CVs of 0.2 µM TNF on MIP-Pt@g-C_3N_4/F-MWCNTs/SPE at a diverse scan rate of 10.0-500.0 mV s^{-1}. (inset); The plot of the I_{pa} vs. $v^{1/2}$ was obtained at MIP-Pt@g-C_3N_4/F-MWCNTs/SPCE.

5.3.6. Chronoamperometry Study

The oxidation of TNF at the Pt@g-C_3N_4/F-MWCNT/SPCE surface was observed using chronoamperometry (Fig. 5.18). Chronoamperometric measurement of diverse concentrations

of TNF at the surface of the Pt@g-C_3N_4/F-MWCNT/SPCE was carried out. From the investigation of chronoamperometric, the diffusion coefficient (D) of TNF was found by using the Cottrell equation[70].

The plots of I vs.$t^{-1/2}$ for diverse concentrations of TNF were found (Fig. 5.18). Using the slope of the plots and the Cottrell equation, D was obtained to be $2.7\times10^{-4}cm^2s^{-1}$.

The value of the electron transfers coefficient (α) of TNF at the Pt@g-C_3N_4/F-MWCNT/SPCE surface was determined using a Tafel plot (Fig. 5.19). The Tafel equation's linear relationship of E vs. log (I) can be expressed (Eq. 5.2). Using relative slopes and the Tafel equation, the value of α was estimated to be ~0.6 at the surface of Pt@g-C_3N_4/F-MWCNT/SPCE.

$$E_{pa} = \frac{2.303\,RT}{(1-\alpha)n_a}\log I \qquad \text{(Eq. 5.2)}$$

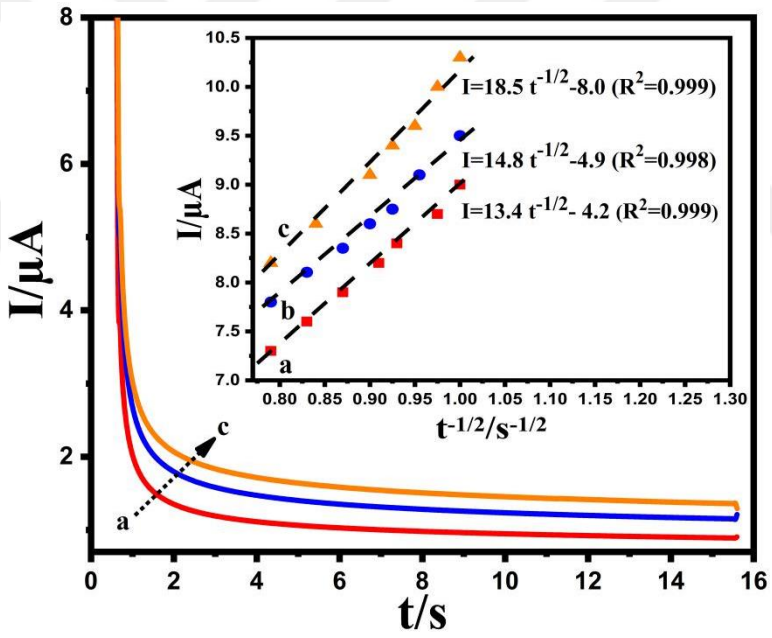

Figure 5.18. (A); Chronoamperograms obtained at MIP-Pt@g-C_3N_4/F-MWCNT/SPCE in the presence of (a) 400, (b) 500 and (c) 600 μM TNF in 0.1 M B-R buffer (pH 5.0). Insert; Cottrell`s plot for the data from the chronoamperograms.

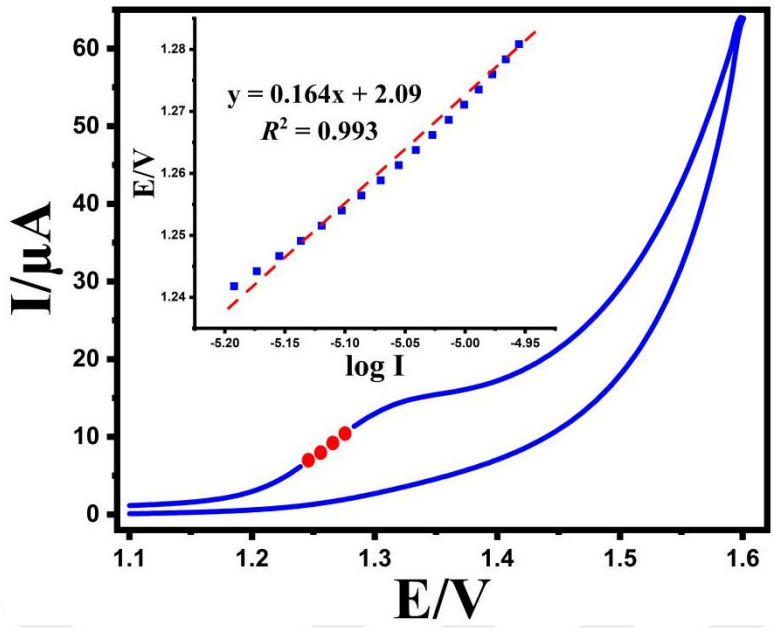

Figure 5.19. Tafel plot at MIP-Pt@g-C_3N_4/F-MWCNTs/SPCE with a scan rate of 100.0 mV/s containing 0.2 μM TNF.

5.4. Analytical Approach for Determination of TNF

The DPV technique was observed to analyze the electrocatalytic performance of MIP-Pt@g-C_3N_4/F-MWCNT/SPCE towards TNF. The analytical performance of TNF was performed on the MIP-Pt@g-C_3N_4/F-MWCNT/SPCE in 0.1 M B-R buffer (pH 5.0) under the optimum experimental states. As shown in Fig. 5.20, excellent linearity of peak current against TNF concentration was observed in the range of 0.005 to 0.69 μM with the linear regression equations expressed as $I = 26.16\ C_{TNF} + 0.977$ ($R^2 = 0.992$). The LOD of TNF at the MIP-Pt@g-C_3N_4/F-MWCNT/SPCE was 0.003 μM (S/N = 3).

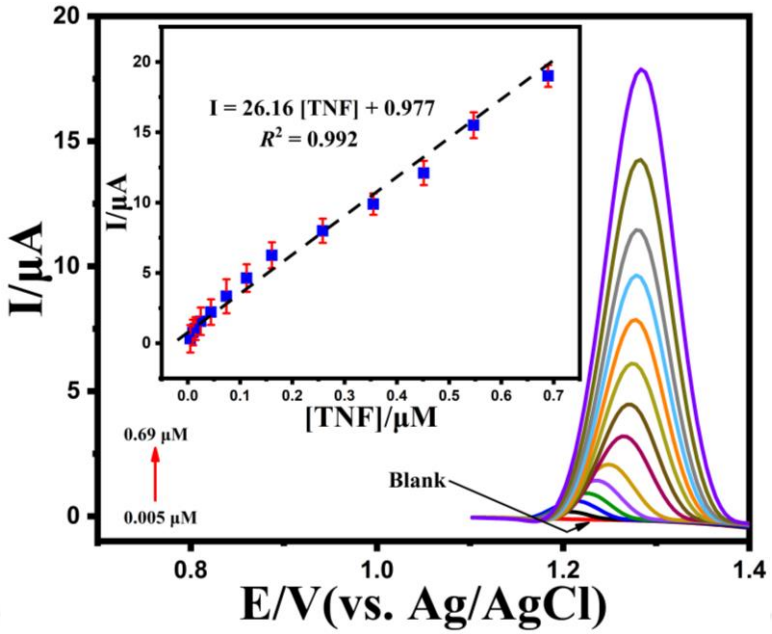

Figure 5.20. DPV with increasing concentrations in 0.1 M B-R buffer pH:5 at Pt@g-C_3N_4/F-MWCNT/SPCE in the range of 0.005-0.69 µM; (inset); the plot of the peak currents vs. TNF concentration.

The strategy and performance of our developed MIP sensor indicated excellent performance, e.g., low LOD and wide linear range compared to the previously reported approaches, which is much better than the existing nanomaterial-based electrochemical sensors for TNF (Table 5.1). Notably, this method considerably cut the preparation cost, simplified the pre-treatment process, and achieved rapid detection compared to the current standard procedures, including HPLC, UV-Vis, and LC-MS. Accordingly, the MIP-Pt@g-C_3N_4/F-MWCNTs/SPCE offers excellent application prospects for TNF determination in complex samples because of its remarkable properties.

Table 5.1. Comparison of the obtained results with similar reports for determination of TNF.

Method	Material	Linear range (μM)	LOD (μM)	Ref.
Aptamer sensor	AptaFET	0.001-0.1	0.012	(Aliakbarinodehi ve ark., 2017)
Voltammetry	BDDE	5.0-100.0	0.56	(Morawska ve ark., 2018)
Voltammetry	Ni-CoS/GQDs	5.0-18.0	0.0121	(Chihava ve ark., 2020)
Voltammetry	BDD	2.38-119	0.62	(Allahverdiyeva ve ark., 2021)
Impedimetric	Ni-CoS-GQDs	-	88.3	(Chihava ve ark., 2018)
Voltammetry	GO/GCE	0.3-30.0	0.048	(Festinger ve ark., 2022)
Voltammetry	MIP-Pt@g-C_3N_4/F-MWCNTs/SPCE	0.005-0.69	0.003	Our work

5.5. Reproducibility

The reproducibility of the developed electrode was valued at a TNF concentration of 0.05 μM. Accordingly, five different electrodes were fabricated independently to determine TNF, and an acceptable reproducibility with an RSD of 2.52% was obtained.

5.6. Repeatability

In order to determine the repeatability, ten successive measurements were performed by DPV in a solution containing 0.05 μM TNF. A relative standard deviation (RSD) of 2.91% was obtained, indicating that the developed sensor has good repeatability.

5.7. Selectivity

It is still considered challenging to detect TNF in complex fluids with high selectivity. The selectivity tests of the present MIP-Pt@g-C_3N_4/F-MWCNT/SPCE were observed in the presence of various interfering agents, such as amino acids and biological species which coexist in the practical fluids. The interference level was observed as the maximum concentration of the interfering substance, resulting in less than a 5.0% error for TNF determination. For 0.05 μM of TNF, over 150-fold interferences did not interfere with the TNF response. The results show that the TNF peak current because of the effect of imprinting of the modified method is not considerably affected by all conventional cations and anions. On the other hand, the high selectivity of the developed electrode stems from the recognition sites of MIP film, matching the template molecule in space size and chemical function, but does not match other interferents. Therefore, the results showed that the MIP-Pt@g-C_3N_4/F-MWCNT/SPCE was selective and indicated binding specificity towards TNF owing to the imprinted effect, suggesting that the modified electrode might find further alternative applications in TNF determination from complex samples without any prior separation.

5.8. Real Sample

The developed electrode was applied to detect TNF in biological and tap water samples to assess its potential in the real aquatic environment (Fig. 5.19). Accuracy and precision were calculated and are shown in Table 5.2. The recoveries of TNF were in the range of 89.2% to 107.7%, with RSD less than 10.0 %, indicating MIP-sensor is a promising tool with good accuracy and selectivity for TNF determination. These results affirm that the suggested method can be used to analyze TNF in real samples.

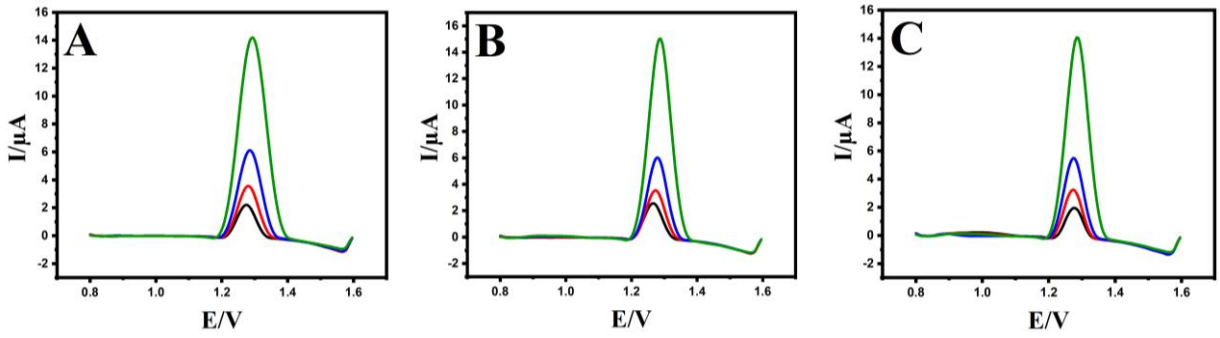

Fig. 5.21. DPV of MIP-Pt@g-C_3N_4/F-MWCNT/SPCE in Human plasma (A), Urine (B), and Tap water with different TNF concentrations.

Table 5.2. The application of the proposed sensor for the determination of TNF.

Sample	Added (μM)	Found (μM)	RSD (%)	Recovery (%)
Human plasma	0.5	0.478	2.59	104.4
	0.2	0.209	0.31	104.8
	0.1	0.104	0.15	104.0
	0.05	0.049	0.29	98.247
Urine	0.5	0.51	1.13	102.04
	0.2	0.206	0.15	103.32
	0.1	0.101	0.08	101.39
	0.05	0.054	0.23	101.62
Tap water	0.5	0.502	0.28	100.58
	0.2	0.195	0.95	97.71
	0.1	0.102	0.56	102.29
	0.05	0.048	0.40	96.91

6. CONCLUSION

In summary, the molecular Imprinting approach generally used for the sensor was also applied in the sensing application of TNF. In this way, we determined TNF in a highly sensitive (LOD: 0.003 μM) and selective way, which brought the possibility of detecting and quantifying the TNF in biological and tap water samples even though it was very low abundant compared to interferences.

Moreover, the developed sensor indicated high selectivity and reliability of visual detection and provided a practical solution for selective recognition and detection of TNF in real samples.

To our best knowledge, this is the first demonstration of the concept of combining Pt@g-C_3N_4/F-MWCNTs and MIPs directly on the screen-printed electrode to detect TNF. The approach offers many attractive advantages such as portability, disposability, low cost, user-friendly protocol, wider linear range, and lower detection limit compared with the previously reported sensors, making the MIP-Pt@g-C_3N_4/F-MWCNTs sensor have the great applicable potential for building innovative MIP-TNF sensors in various fields.

The analytical performances of the electrochemical sensors have been developed for TNF and compared with similar studies carried out so far and it has been concluded that sensitive electrochemical sensors have been developed within the scope of the thesis project. In addition, selectivity and % recovery studies were performed with a developed electrochemical sensor. In selectivity studies, TNF was analyzed in the presence of potential interference substances by the as-fabricated electrode. Electrochemical analysis of TNF from human plasma, urine, and tap water samples has been successfully applied. The obtained selectivity and % recovery results showed that the electrochemical sensors developed by us are selective towards Tenofovir. In conclusion, we suggest that the sensitive and selective MIP-Pt@g-C_3N_4/F-MWCNTs that we have developed for the direct determination of Tenofovir from real samples can be used as alternative analytical methods in the analysis of TNF as the point of care diagnostics.

ABSTRACT

Development of a Disposable MIP-based Electrochemical Sensor for Determination of the Antiviral Drug

The application of molecularly imprinted polymer (MIP) electrochemical sensors as a sensing alternative to directly detect Tenofovir (TNF) as an antiviral medication in biological samples is demonstrated in this thesis. The crystallinity, surface morphology, bonding, and functional groups of MIP-platinum nanoparticles/graphitic carbon nitride/functionalized multiwalled carbon nanotubes (MIP-Pt@g-C_3N_4/F-MWCNTs) were investigated using X-ray diffraction (XRD), scanning electron microscopy (SEM), Fourier transform infrared spectroscopy (FTIR), BET-N_2 surface analysis, ultraviolet-visible spectroscopy (UV-Vis) and atomic force microscopy (AFM). Moreover, the electrochemical properties of the developed sensor were studied using electrochemical impedance spectroscopy (EIS), cyclic voltammetry (CV), differential pulse voltammetry (DPV), and chronoamperometry (CA). In this study, we designed a MIP-type electrochemical sensor capable of rapidly detecting TNF with an ultra-low detection limit (LOD) of 0.0030 μM within a wide linear concentration range from 0.005 to 0.69 μM. In the existence of interferences, a TNF imprinted electrode was used to detect TNF in urine, human plasma, and tap water as real samples with high sensitivity and satisfactory recovery. The modified electrode was also demonstrated high performance for stability, repeatability, reproducibility, and reusability. Hence, the developed electrochemical sensor having high stability, repeatability, reproducibility, and reusability were presented in this study for TNF determination. Based on the results, MIP-Pt@g-C_3N_4/F-MWCNTs/SPE can be utilized as a novel method to detect antiviral agents such as TNF.

Keywords: Molecularly imprinted sensor, Voltammetry, Tenofovir, Biological samples

ÖZET

Antiviral İlacın Belirlenmesi İçin Tek Kullanımlık Bir MİP Tabanlı Elektrokimyasal Sensörün Geliştirilmesi

Tez çalışmasında, antiviral etkili Tenofovir etken maddesi, moleküler baskılı polimer (MIP) elektrokimyasal sensörler kullanılarak biyolojik numunelerden doğrudan analiz edilmiştir. MIP-platin nanopartiküller/grafik karbon nitrür/fonksiyonelleştirilmiş çok duvarlı karbon nanotüplerin (MIP-Pt@g-C_3N_4/F-MWCNTs) kristalliği, yüzey morfolojisi, bağlanması ve fonksiyonel grupları X-ışını kırınımı (XRD) taramalı elektron mikroskopi (SEM), Fourier dönüşümlü kızılötesi spektroskopisi (FTIR), BET-N_2 yüzey analizi, ultraviyole görünür spektroskopi (UV-Vis) ve atomik kuvvet mikroskobu (AFM) kullanılarak araştırılmıştır. Ek olarak geliştirilen sensörlerin elektrokimyasal özellikleri elektrokimyasal impedans spektroskopi (EIS), dönüşümlü voltametri (CV), diferansiyel puls voltametri (DPV) ve kronoamperometri (CA) yöntemleri ile çalışılmıştır. Çalışmamızda, 0,005 ila 0,69 µM arasında geniş bir doğrusal konsantrasyon aralığında 0,0030 µM ultra-düşük tespit limiti (LOD) ile TNF'yi hızla analiz edebilen MIP tipi bir elektrokimyasal sensör tasarlanmıştır. TNF, baskılı elektrot kullanılarak idrarda, insan plazmasında ve suda, girişim yapan maddelerin varlığında yüksek hassasiyet ve yüzde geri kazanım değerleri ile analiz edilmiştir. Modifiye elektrot ayrıca kararlılık, tekrarlanabilirlik ve tekrar kullanılabilirlik için yüksek performans göstermiştir. Sonuç olarak, TNF tayini için geliştirilen elektrokimyasal sensör yüksek kararlılık, tekrarlanabilirlik ve tekrar kullanılabilirlik özelliklerine sahip olarak bulunmuştur çalışmada sunulmuştur. Sonuçlara göre, MIP-Pt@g-C_3N_4/F-MWCNTs/SPE, TNF gibi antiviral ajanları saptamak için yeni bir yöntem olarak kullanılabilir.

Anahtar Sözcükler: Moleküler baskılı sensör, Voltametri, Tenofovir, Biyolojik numune

REFERENCES

ALIAKBARINODEHI N, JOLLY P, BHALLA N, MIODEK A, DE MICHELI G, ESTRELA P, CARRARA S (2017). Aptamer-based field-effect biosensor for tenofovir detection. *Scientific reports,* **7**(1): 1-10.

ALLAHVERDIYEVA S, PıNAR PT, YARDıM Y, ŞENTÜRK Z (2021). First report for the electrochemical investigation of a new HIV integrase inhibitor dolutegravir: Its voltammetric determination in tablet dosage forms and human urine using a boron-doped diamond electrode. *Diamond and Related Materials,* **114**: 108332.

ALONZO AA, REYNOLDS NR (1995). Stigma, HIV and AIDS: An exploration and elaboration of a stigma trajectory. *Social science & medicine,* **41**(3): 303-315.

ANDERSSON LI (2000). Molecular imprinting: developments and applications in the analytical chemistry field. *Journal of Chromatography B: Biomedical Sciences and Applications,* **745**(1): 3-13.

ANSARI S, KARIMI M (2017). Recent configurations and progressive uses of magnetic molecularly imprinted polymers for drug analysis. *Talanta,* **167**: 470-485.

AYERDURAI V, CIEPLAK M, NOWORYTA KR, GAJDA M, ZIMINSKA A, SOSNOWSKA M, PIECHOWSKA J, BOROWICZ P, LISOWSKI W, SHAO S (2021). Electrochemical sensor for selective tyramine determination, amplified by a molecularly imprinted polymer film. *Bioelectrochemistry*, **138**: 107695.

BALFOUR JR HH (1999). Antiviral drugs. *New England Journal of Medicine,* **340**(16): 1255-1268.

BAŚ B, KOWALSKI Z (2002). Preparation of silver surface for mercury film electrode of prolonged analytical application. *Electroanalysis: An International Journal Devoted to Fundamental and Practical Aspects of Electroanalysis,* **14**(15-16): 1067-1071.

BLANCO-LOPEZ M, GUTIERREZ-FERNANDEZ S, LOBO-CASTANON M, MIRANDA-ORDIERES A, TUNON-BLANCO P (2004). Electrochemical sensing with electrodes modified with molecularly imprinted polymer films. *Analytical and bioanalytical chemistry,* **378**(8): 1922-1928.

BRANGER C, MEOUCHE W, MARGAILLAN A (2013). Recent advances on ion-imprinted polymers. *Reactive and Functional Polymers,* **73**(6): 859-875.

CACHO C, TURIEL E, MARTÍN-ESTEBAN A, AYALA D, PÉREZ-CONDE C (2006). Semi-covalent imprinted polymer using propazine methacrylate as template molecule for the clean-up of triazines in soil and vegetable samples. *Journal of chromatography A,* **1114**(2): 255-262.

CHIHAVA R, APATH D, MOYO M, SHUMBA M, CHITSA V, TSHUMA P (2020). One-pot synthesized nickel-cobalt sulfide-decorated graphene quantum dot composite for simultaneous electrochemical determination of antiretroviral drugs: lamivudine and tenofovir disoproxil fumarate. *Journal of Sensors,* **2020**.

CHIHAVA R, MOYO M, SHUMBA M. (2018). *Impedimetric determination of antiretroviral drugs on a modified glassy carbon electrode.* Paper presented at the 2018 IEEE SENSORS.

DEL SOLE R, LAZZOI MR, ARNONE M, SALA FD, CANNOLETTA D, VASAPOLLO G (2009). Experimental and computational studies on non-covalent imprinted microspheres as recognition system for nicotinamide molecules. *Molecules,* **14**(7): 2632-2649.

DEROCO PB, ROCHA-FILHO RC, FATIBELLO-FILHO O (2018). A new and simple method for the simultaneous determination of amoxicillin and nimesulide using carbon black within a dihexadecylphosphate film as electrochemical sensor. *Talanta,* **179**: 115-123.

DUESBERG PH (1989). Human immunodeficiency virus and acquired immunodeficiency syndrome: Correlation but not causation. *Proceedings of the National Academy of Sciences,* **86**(3): 755-764.

FERNANDEZ-FERNANDEZ B, MONTOYA-FERRER A, SANZ AB, SANCHEZ-NINO MD, IZQUIERDO MC, POVEDA J, SAINZ-PRESTEL V, ORTIZ-MARTIN N, PARRA-RODRIGUEZ A, SELGAS R (2011). Tenofovir nephrotoxicity: 2011 update. *AIDS research and treatment,* **2011**.

FESTINGER N, SPILAREWICZ-STANEK K, BOROWCZYK K, GUZIEJEWSKI D, SMARZEWSKA S (2022). Highly Sensitive Determination of Tenofovir in Pharmaceutical Formulations and Patients Urine—Comparative Electroanalytical Studies Using Different Sensing Methods. *Molecules,* **27**(6): 1992.

GEBRESLASSIE G, BHARALI P, CHANDRA U, SERGAWIE A, BORUAH PK, DAS MR, ALEMAYEHU E (2019). Novel g-C3N4/graphene/NiFe2O4 nanocomposites as magnetically separable visible light driven photocatalysts. *Journal of Photochemistry and Photobiology A: Chemistry,* **382**: 111960.

GIMENEZ J, CASSAGNAU P, MICHEL A (2000). Bulk polymerization of ε-caprolactone: Rheological predictive laws. *Journal of Rheology,* **44**(3): 527-547.

GOPI PK, SUBBURAJ S, CHEN T-W, CHEN S-M, AL-SHAALAN NH, OULADSMANE M, ALI MA, LIU X (2021). An expedition of WBiVO4 blended f-MWCNTs nanocomposite for enhanced electrochemical detection of non-steroidal anti-inflammatory drug acetaminophenol. *Colloids and Surfaces A: Physicochemical and Engineering Aspects,* **618**: 126454.

HASHIM SN, BOYSEN RI, SCHWARZ LJ, DANYLEC B, HEARN MT (2014). A comparison of covalent and non-covalent imprinting strategies for the synthesis of stigmasterol imprinted polymers. *Journal of chromatography A,* **1359**: 35-43.

HWANG C-C, LEE W-C (2002). Chromatographic characteristics of cholesterol-imprinted polymers prepared by covalent and non-covalent imprinting methods. *Journal of chromatography A,* **962**(1-2): 69-78.

KADIVAR M, ALIAKBAR A (2019). A new composite based on graphene oxide-poly 3-aminophenol for solid-phase microextraction of four triazole fungicides in water and fruit juices prior to high-performance liquid chromatography analysis. *Food chemistry,* **299**: 125127.

KADIVAR M, ALIAKBAR A (2021). A molecularly imprinted poly 2-aminophenol–gold nanoparticle–reduced graphene oxide composite for electrochemical determination of flutamide in environmental and biological samples. *Analytical Methods,* **13**(4): 536-551.

KANDAGAL P, MANJUNATHA D, SEETHARAMAPPA J, KALANUR S (2008). RP-HPLC method for the determination of tenofovir in pharmaceutical formulations and spiked human plasma. *Analytical letters,* **41**(4): 561-570.

KARIMI-MALEH H, AROTIBA OA (2020). Simultaneous determination of cholesterol, ascorbic acid and uric acid as three essential biological compounds at a carbon paste electrode modified with copper oxide decorated reduced graphene oxide nanocomposite and ionic liquid. *Journal of colloid and interface science,* **560**: 208-212.

KASTURI S, TORATI SR, EOM YJ, AHMAD S, LEE B-J, YU J-S, KIM C (2020). Real-time monitored photocatalytic activity and electrochemical performance of an rGO/Pt nanocomposite synthesized via a green approach. *RSC Advances,* **10**(23): 13722-13731.

KUMAR VR, REDDY BPB, KUMAR BR, SREEKANTH K, BABU KN (2013). High throughput LC–MS/MS method for simultaneous determination of zidovudine, lamivudine and nevirapine in human plasma. *Journal of Chromatography B,* **921**: 9-14.

LEITE FRF, SANTOS WDJR, KUBOTA LT (2014). Selective determination of caffeic acid in wines with electrochemical sensor based on molecularly imprinted siloxanes. *Sensors and Actuators B: Chemical,* **193**: 238-246.

LI Y, TANG L, LI J (2009). Preparation and electrochemical performance for methanol oxidation of Pt/graphene nanocomposites. *Electrochemistry Communications,* **11**(4): 846-849.

LOWENTHAL ED, BAKEERA-KITAKA S, MARUKUTIRA T, CHAPMAN J, GOLDRATH K, FERRAND RA (2014). Perinatally acquired HIV infection in adolescents from sub-Saharan Africa: a review of emerging challenges. *The Lancet infectious diseases,* **14**(7): 627-639.

MAHMOUDIAN M, ALIAS Y, WOI PM, YOUSEFI R, BASIRUN W (2020). An electrochemical sensor based on Pt/g-C3N4/polyaniline nanocomposite for detection of Hg2+. *Advanced Powder Technology,* **31**(8): 3372-3380.

MARTÍN-ESTEBAN A (2013). Molecularly-imprinted polymers as a versatile, highly selective tool in sample preparation. *TrAC Trends in Analytical Chemistry,* **45**: 169-181.

MENON S, JESNY S, KUMAR KG (2018). A voltammetric sensor for acetaminophen based on electropolymerized-molecularly imprinted poly (o-aminophenol) modified gold electrode. *Talanta,* **179**: 668-675.

MOHAJERI SA, KARIMI G, AGHAMOHAMMADIAN J, KHANSARI MR (2011). Clozapine recognition via molecularly imprinted polymers; bulk polymerization versus precipitation method. *Journal of Applied Polymer Science,* **121**(6): 3590-3595.

MORAWSKA K, POPŁAWSKI T, CIESIELSKI W, SMARZEWSKA S (2018). Electrochemical and spectroscopic studies of the interaction of antiviral drug Tenofovir with single and double stranded DNA. *Bioelectrochemistry,* **123**: 227-232.

NEVASE PA, NIMJE HM, OSWAL RJ, ANTRE RV, KSHIRSAGAR SS (2011). Uv Spectrophotometric Method For Estimation Of Tenofovir Disoproxil Fumarate Tablet Dosage Form. *Int J Pharm Res Dev,* **3**: 73-75.

OZCELIKAY G, DOGAN-TOPAL B, OZKAN SA (2017). Electrochemical characteristics of tenofovir and its determination in dosage form by electroanalytical methods. *Rev. Roum. Chim,* **62**(6-7): 569-578.

PEACOCK-VILLADA E, RICHARDSON BA, JOHN-STEWART GC (2011). Post-HAART outcomes in pediatric populations: comparison of resource-limited and developed countries. *Pediatrics,* **127**(2): e423-e441.

PUZIO K, DELÉPÉE R, VIDAL R, AGROFOGLIO LA (2013). Combination of computational methods, adsorption isotherms and selectivity tests for the conception of a mixed non-covalent–semi-covalent molecularly imprinted polymer of vanillin. *Analytica chimica acta,* **790**: 47-55.

RENKECZ T, MISTLBERGER GN, PAWLAK M, HORVÁTH V, BAKKER E (2013). Molecularly imprinted polymer microspheres containing photoswitchable spiropyran-based binding sites. *ACS applied materials & interfaces,* **5**(17): 8537-8545.

SAHOO RC, LU H, GARG D, YIN Z, MATTE HR (2022). Bandgap engineered g-C3N4 and its graphene composites for stable photoreduction of CO2 to methanol. *Carbon*.

SHAABANI N, CHAN NW, JEMERE AB (2021). A molecularly imprinted sol-gel electrochemical sensor for naloxone determination. *Nanomaterials,* **11**(3): 631.

SIBERRY GK, LEISTER E, JACOBSON DL, FOSTER SB, SEAGE III GR, LIPSHULTZ SE, PAUL ME, PURSWANI M, COLIN AA, SCOTT G (2012). Increased risk of asthma and atopic dermatitis in perinatally HIV-infected children and adolescents. *Clinical immunology,* **142**(2): 201-208.

SONG Z, LI J, LU W, LI B, YANG G, BI Y, ARABI M, WANG X, MA J, CHEN L (2021). Molecularly imprinted polymers based materials and their applications in chromatographic and electrophoretic separations. *TrAC Trends in Analytical Chemistry*: 116504.

SPELTINI A, SCALABRINI A, MARASCHI F, STURINI M, PROFUMO A (2017). Newest applications of molecularly imprinted polymers for extraction of contaminants from environmental and food matrices: A review. *Analytica chimica acta,* **974**: 1-26.

SPIRESCU VA, CHIRCOV C, GRUMEZESCU AM, ANDRONESCU E (2021). Polymeric nanoparticles for antimicrobial therapies: An up-to-date overview. *Polymers*, **13**(5): 724.

SUN J, FENG S, FENG S (2020). Hydrothermally synthesis of MWCNT/N-TiO2/UiO-66-NH2 ternary composite with enhanced photocatalytic performance for ketoprofen. *Inorganic Chemistry Communications*, **111**: 107669.

SUN X, JIAN Y, WANG H, GE S, YAN M, YU J (2019). Ultrasensitive microfluidic paper-based electrochemical biosensor based on molecularly imprinted film and boronate affinity sandwich assay for glycoprotein detection. *ACS Applied Materials & Interfaces*, **11**(17): 16198-16206.

TAMAYO F, TURIEL E, MARTÍN-ESTEBAN A (2007). Molecularly imprinted polymers for solid-phase extraction and solid-phase microextraction: Recent developments and future trends. *Journal of chromatography A*, **1152**(1-2): 32-40.

TOMPA DR, IMMANUEL A, SRIKANTH S, KADHIRVEL S (2021). Trends and strategies to combat viral infections: A review on FDA approved antiviral drugs. *International journal of biological macromolecules*, **172**: 524-541.

TURIEL E, MARTIN-ESTEBAN A (2004). Molecularly imprinted polymers: towards highly selective stationary phases in liquid chromatography and capillary electrophoresis. *Analytical and bioanalytical chemistry*, **378**(8): 1876-1886.

VASAPOLLO G, SOLE RD, MERGOLA L, LAZZOI MR, SCARDINO A, SCORRANO S, MELE G (2011). Molecularly imprinted polymers: present and future prospective. *International journal of molecular sciences*, **12**(9): 5908-5945.

WANG C, HOWELL M, RAULJI P, DAVIS Y, MOHAPATRA S (2011). Preparation and characterization of molecularly imprinted polymeric nanoparticles for atrial natriuretic peptide (ANP). *Advanced functional materials*, **21**(23): 4423-4429.

WANG S, SUN G, CHEN Z, LIANG Y, ZHOU Q, PAN Y, ZHAI H (2018). Constructing a novel composite of molecularly imprinted polymer-coated AuNPs electrochemical sensor for the determination of 3-nitrotyrosine. *Electrochimica Acta,* **259**: 893-902.

WASSNER C, BRADLEY N, LEE Y (2020). A Review and clinical understanding of tenofovir: tenofovir disoproxil fumarate versus tenofovir alafenamide. *Journal of the International Association of Providers of AIDS Care (JIAPAC),* **19**: 2325958220919231.

XU J, ZHANG L, SHI R, ZHU Y (2013). Chemical exfoliation of graphitic carbon nitride for efficient heterogeneous photocatalysis. *Journal of Materials Chemistry A,* **1**(46): 14766-14772.

YOSHIKAWA M, THARPA K, DIMA S-O (2016). Molecularly imprinted membranes: past, present, and future. *Chemical reviews,* **116**(19): 11500-11528.

ZHANG H, YE L, MOSBACH K (2006). Non-covalent molecular imprinting with emphasis on its application in separation and drug development. *Journal of Molecular Recognition: An Interdisciplinary Journal,* **19**(4): 248-259.

ZHANG L, WEN Y, YAO Y, XU J, DUAN X, ZHANG G (2014). Synthesis and characterization of PEDOT derivative with carboxyl group and its chemo/bio sensing application as nanocomposite, immobilized biological and enhanced optical materials. *Electrochimica Acta,* **116**: 343-354.

ZHAO H, YU H, QUAN X, CHEN S, ZHAO H, WANG H (2014). Atomic single layer graphitic-C 3 N 4: fabrication and its high photocatalytic performance under visible light irradiation. *RSC advances,* **4**(2): 624-628.